iScience

Article

Alterations in ether phospholipids metabolism activate the conserved UPR-Xbp1- PDIA3/ERp60 signaling to maintain intestinal homeostasis

Graphical abstract

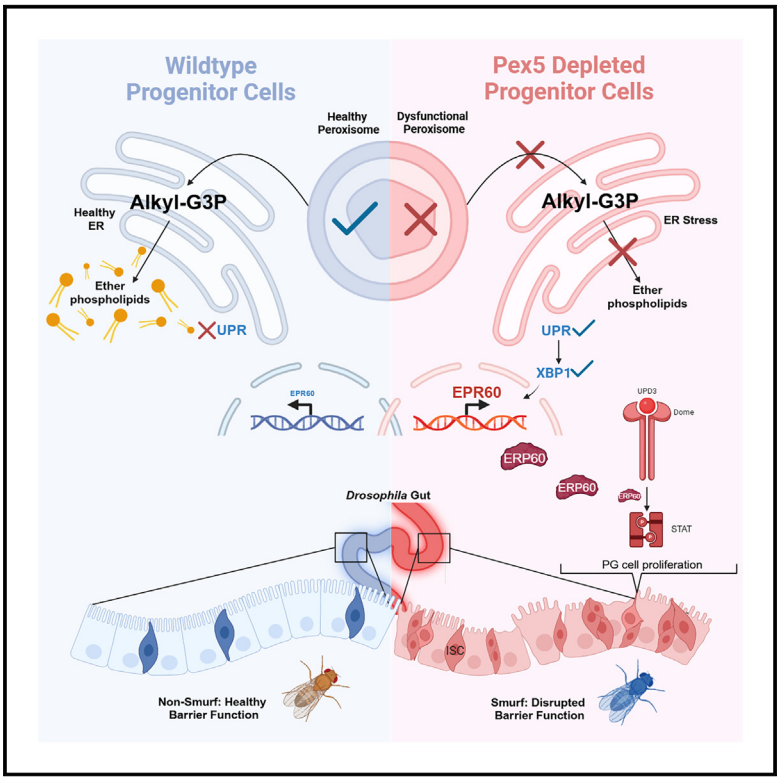

Highlights

- Ether phospholipids metabolism is required for intestinal homeostasis
- Dysfunction in peroxisomal ether phospholipids metabolism triggers Xbp1 and the UPR
- ERp60, the ortholog of mammalian PDIA3, regulates intestinal progenitor number
- Xbp1-ERp60 induction affects intestinal homeostasis only in male adult Drosophila

Authors

Stephanie Makdissi, Rihab Loudhaief, Smitha George, ..., Yizhu Mu, Brendon D. Parsons, Francesca Di Cara

Correspondence

dicara@dal.ca

In brief

Cell biology, Lipidomics, Molecular biology

Makdissi et al., 2025, iScience *28*, 111946
March 21, 2025
https://doi.org/10.1016/j.isci.2025.111946

CellPress

iScience

CellPress
OPEN ACCESS

Article

Alterations in ether phospholipids metabolism activate the conserved UPR-Xbp1- PDIA3/ERp60 signaling to maintain intestinal homeostasis

Stephanie Makdissi,[1,2,4] Rihab Loudhaief,[1,2,4] Smitha George,[1,2] Tabatha Weller,[1] Minna Salim,[1] Ahsan Malick,[1,2] Yizhu Mu,[1,2] Brendon D. Parsons,[3] and Francesca Di Cara[1,2,5,*]

[1]Department of Microbiology and Immunology, Faculty of Medicine, Dalhousie University, Halifax, NS, Canada
[2]Department of Pediatrics, Dalhousie University, Izaak Walton Killam (IWK) Health Centre, Halifax, NS, Canada
[3]Department of Laboratory Medicine & Pathology, Faculty of Medicine & Dentistry -University of Alberta, Edmonton, AB, Canada
[4]These authors contributed equally
[5]Lead contact
*Correspondence: dicara@dal.ca
https://doi.org/10.1016/j.isci.2025.111946

SUMMARY

Intestinal epithelium regeneration and homeostasis must be tightly regulated. Alteration of epithelial homeostasis is a major contributing factor to diseases such as colorectal cancer and inflammatory bowel diseases. Many pathways involved in epithelial regeneration have been identified, but more regulators remain undiscovered. Metabolism has emerged as an overlooked regulator of intestinal epithelium homeostasis. Using the model organism *Drosophila melanogaster*, we found that ether lipids metabolism is required to maintain intestinal epithelial homeostasis. Its dysregulation in intestinal progenitors causes the activation of the unfolded protein response of the endoplasmic reticulum (UPR) that triggers Xbp1 and upregulates the conserved disulfide isomerase PDIA3/ERp60. Activation of the Xbp1-ERp60 signaling causes Jak/Stat-mediated increase in progenitor cells, compromising epithelial barrier function and survival in males but not females. This study identified ether lipids-PDIA3/ERp60 as a key regulator of intestinal progenitor homeostasis in health that, if altered, causes pathological conditions in the intestinal epithelium.

INTRODUCTION

All epithelial layers need to preserve homeostasis to execute their function and maintain a healthy physiological status. Epithelial homeostasis is achieved by the precise balance of epithelial stem cell/progenitor (PG) proliferation and differentiation. The intestinal epithelium is the largest epithelium of the body.[1,2] It can digest and absorb nutrients and promote endocrine and immune regulation while keeping a healthy relationship with the beneficial commensals. The intestinal epithelium has a limited lifespan of about 4–5 days, and it has to be constantly replenished to prevent disruption of the barrier function. Intestinal stem cells (ISCs) continuously self-renew and give rise to enteroblasts (EB) that can go through differentiation to originate specialized absorptive or secretory epithelial cells and maintain intestinal epithelium functions.[3] Intrinsic pressures from genetic or epigenetic sources and extrinsic pressures imposed by pathogens, commensals, or xenobiotic insults can disrupt epithelial homeostasis,[4–7] promoting excessive proliferation and driving diseases such as inflammatory bowel disease and colorectal cancer.[8]

To date, many signaling pathways that regulate ISC homeostasis, such as Wingless-related integration site (WNT), Janus kinase/signal transducers and activators of transcription (JAK/STAT), Hippo pathway (Hpo), Notch signaling, epidermal growth factor receptor (EGFR), insulin receptor signaling (InRs), and Hedgehog (Hh) signaling, have been identified in *Drosophila* and mammals.[6,9–12] Although these studies have deepened our understanding of the complex mechanisms of ISC homeostasis, many more pathways remain to be explored. Metabolic regulation of the ISC niche in physiological conditions and under stress has emerged as a crucial regulator of ISC proliferation and differentiation and as an integrator of environmental cues[13–15] that impact ISC homeostasis. For instance, increased glycolysis and mitochondrial fatty acid oxidation promote stem cell activation in healthy and injured states.[16,17] It was demonstrated in *Drosophila* and mammals that the mitochondrial tricarboxylic acid (TCA) cycle, oxidative phosphorylation (OXPHOS) pathway, and ATP production support the proliferation of ISC under regenerative stimuli[18–20] and in murine models of intestinal inflammatory conditions.[21] Moreover, a cross-talk between glycolysis and mitochondrial fatty acid β-oxidation regulates the EGFR-mediated ISC division and differentiation in *Drosophila*,[22] and fatty acid oxidation is required for survival and renewal of the intestinal epithelium in mice,[23] highlighting the important role of mitochondrial metabolism in ISC differentiation.

Cellular metabolism is orchestrated by controlled synergy between organelles.[24] Recent studies suggest that organelles such

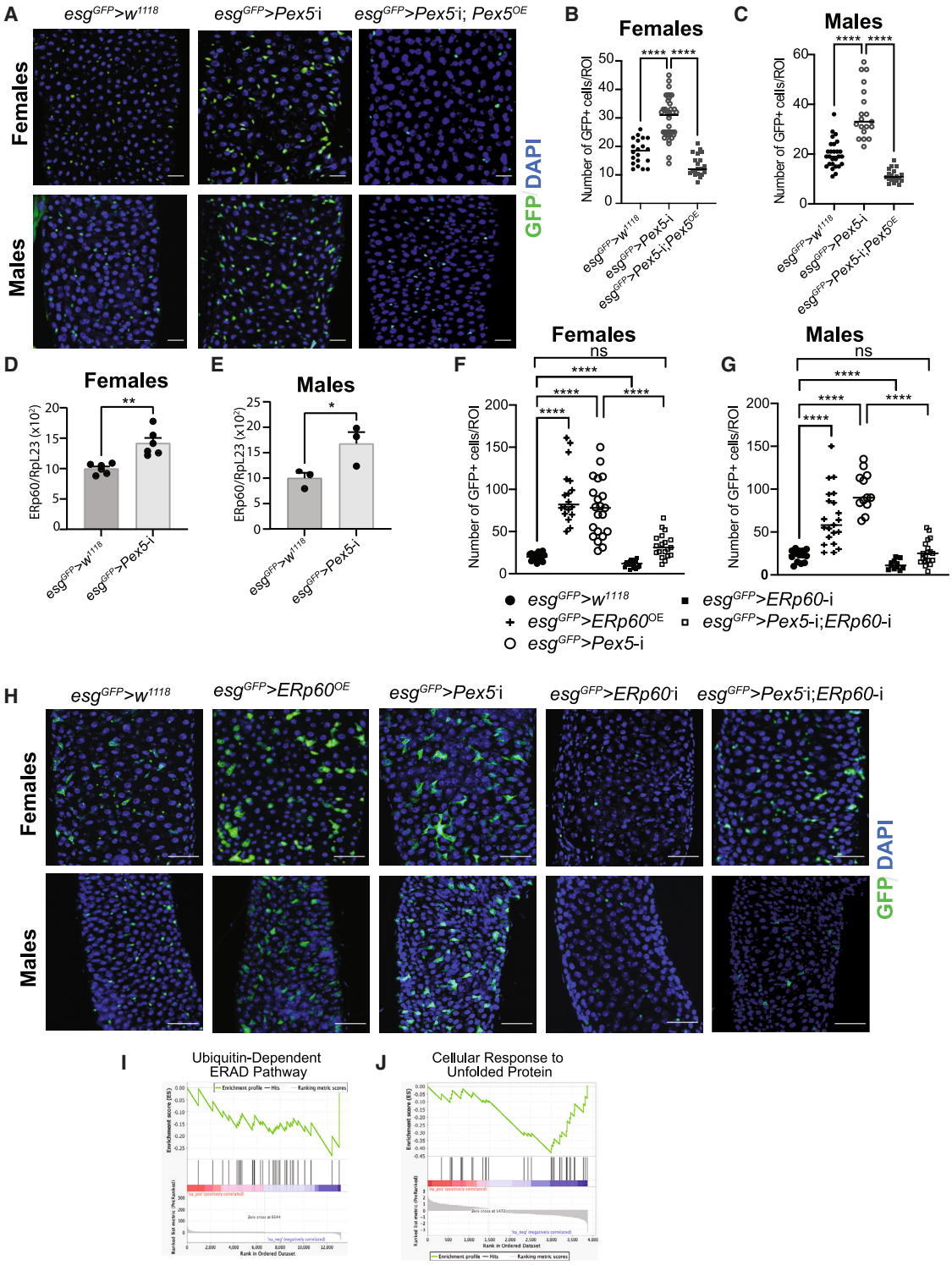

Figure 1. Depletion of *Pex5* in progenitor cells leads to the upregulation of ER-stress response ERp60 and an increase in esg^{+} cells in adult guts

(A) Representative images showing esg^{GFP} (green) cells in *Drosophila* female and male adult posterior midgut regions of *esg^{GFP}>w^{1118}* control strain and *esg^{GFP}>Pex5-i* strain with dysfunctional peroxisomes in progenitor cells. Scale bar, 20 μm.

(B and C) The dot plots represent the number of esg^{GFP} cells per region of interest (ROI) in (B) female or (C) male adult posterior midguts of flies of the reported genotypes. *n* = 15–35.

(legend continued on next page)

as the endoplasmic reticulum (ER) and peroxisome also directly regulate signaling that controls ISC proliferation through their metabolism.[25]

Most studies have characterized glycolysis and mitochondrial metabolism directing ISC homeostasis, whereas much less is known about the role of other organelles and their metabolism in ISC regulation.

Using the genetically sophisticated model organism *Drosophila melanogaster*, a proven valuable model organism to identify mechanisms controlling ISC homeostasis in health and diseases,[3,26] we investigated the role of peroxisomal metabolism in controlling ISC homeostasis. Peroxisomes are essential metabolic organelles present virtually in every eukaryotic cell and the only site where very long-chain fatty acid (VLCFA) β-oxidation, α-oxidation of branched-chain fatty acids, and synthesis of ether lipid precursors occur.[27] Genetic mutations that affect genes encoding for the so-called Peroxins (Pex) involved in peroxisomal biogenesis and function lead to cellular metabolic dysfunctions in all eukaryotes.[28] Previous evidence has shown that RNA interference (RNAi)-mediated depletion of *Peroxin5* (*Pex5*) in PGs[10] results in the increased proliferation and accumulation of PGs in the posterior midguts of adult *Drosophila* under physiological conditions[29] and in the presence of oxidative stress.[30]

Here, we demonstrate that the reduction of peroxisomal ether lipid metabolism prompts the ER stress response in PGs and triggers the unfolded protein response (UPR)[31,32] to drive excess PG proliferation in the attempt to restore intestinal epithelial homeostasis. Ether lipids are essential components of every biomembrane, and their synthesis happens between the peroxisome and the ER.[33] Alteration of lipid metabolism can trigger ER stress[34,35] in stem cells,[36] and UPR activation was previously linked to intestinal homeostasis in *Drosophila melanogaster*.[37,38]

ER stress is sensed by the three main ER sensor proteins in *Drosophila* as in mammalian cells: inositol-requiring enzyme 1 (IRE1), protein kinase R (PKR)-like ER kinase (PERK), and activating transcription factor 6 (ATF6). Upon ER stress, each protein controls distinct branches of UPR that regulate unique transcriptional or translational programs,[39,40] alleviating ER stress primarily via three mechanisms.[41] These mechanisms aim to (1) increase the protein-folding capacity of the ER by inducing the transcription of various genes encoding molecular chaperones and folding enzymes; (2) attenuate protein translation to reduce the burden on ER; and (3) transport misfolded proteins from the ER back to the cytosol, for degradation by the proteasome, a process called ER-associated protein degradation (ERAD).

Previous research reported that peroxisomal dysfunction in murine global *Pex2*$^{-/-}$ knockout drives ER stress response in hepatic cells, leading to PERK activation and deregulation of sterol metabolism.[42,43] However, why peroxisomal dysfunction drives the ER stress response was not mechanistically defined, nor was the activation of the other sensors of the UPR in hepatic cells or any other cell or organism.

We found that alteration of peroxisomal ether phospholipid metabolism stalls the production of phospholipid species essential for the cells, triggering the Xbp1 branch of the UPR response.[44] Xbp1 drives the expression of ERp60, the ortholog of protein disulfide isomerase A3 (PDIA3), a pleiotropic member of the PDIs family involved in protein folding.[45] PDIA3 has been implicated in the regulation of various cellular signaling in the ER and other cellular compartments, including the nucleus, the plasma membrane, and mitochondria,[45] controlling many physiological and pathological signaling.[45–48] We demonstrated that ERp60 is a regulator of PG homeostasis and responds to ether lipid metabolic shifts.

Our data provide evidence of an inter-talk between peroxisome and ER lipid metabolism to control ISC homeostasis and intestinal regeneration. Considering the importance of metabolism and UPR response in cancer and intestinal inflammatory diseases,[49] the discovery of a peroxisome-ER-ether lipid-ERp60 axis opens avenues of exploration for future interventions to control cancer and chronic intestinal inflammation.

RESULTS

Depletion of *Pex5* in *Drosophila* intestinal progenitor cells leads to the activation of *ERp60*, a novel regulator of PG cell number

Pex5 encodes for a cytoplasmic receptor needed to form metabolically functional peroxisomes.[50] We previously reported that the depletion of *Pex5* by *in vivo* RNA interference (RNAi) in intestinal PG (ISC and EB) increased the number of midgut PG in adult female and male flies due to accelerated PG proliferation as demonstrated by an increase in phospho-histone3 (PH3), a specific marker for mitotic cells.[29] This increase in PG cells did not affect differentiation as the ratio of enterocytes (EC) to enteroendocrine cells (EE) did not change compared to what was observed in control age-matched guts.[29] To determine how peroxisomal dysfunction leads to a significant increase in PG proliferation (Figures 1A–1C), we performed RNA sequencing (RNAseq) of intestinal PG isolated by fluorescence-activated cell sorting (FACS) from the midguts of 10-day-old pooled male and female adult flies (Figure S1A). We used flies encoding the *esgGal4,UAS-GFP;tub-Gal80*^{ts} (*esg*^{GFP}) driver[10] and compared the transcriptional profiles of PG from a control strain (*esg*^{GFP}>*w*^{1118}) to the *Pex5* RNAi strain (esg^{GFP}>*Pex5*-i),

(D) The bar graph represents the relative expression of ERp60 transcript versus Rpl23 in *esg*^{GFP}>*w*^{1118} and *esg*^{GFP}>*Pex5*-i female adult midguts. $n = 6$.
(E) The bar graph represents the relative expression of ERp60 transcript versus Rpl23 in *esg*^{GFP}>*w*^{1118} and *esg*^{GFP}>*Pex5*-i male adult midguts. $n = 3$.
(F and G) The dot plots represent the number of esg^{GFP} cells per ROI in the posterior midguts of (F) female or (G) male flies of the reported genotypes. $n = 15–20$.
(H) Fluorescent microscopic images showing esg^{GFP} cells (green) in midgut regions of adult female (top panels) and male (bottom panel) flies of the reported genotypes. Scale bar, 50 μm.
(I and J) Select GSEA of differentially expressed genes in *esg*^{GFP}>*Pex5-i* versus *esg*^{GFP}>*w*^{1118} progenitors from adult male and female intestines that were significantly enriched in functional categories of (I) ubiquitin-dependent ERAD pathway and (J) response to unfolded proteins. In every image, the DNA was stained with DAPI (blue). The error bars represent the standard deviation of the mean. Statistical significance was calculated using unpaired t tests in (D) and (E) and one-way ANOVA tests in (B, C, F, and G). ****$p < 0.0001$; **$p < 0.01$; *$p < 0.05$; ns, not significant. See also Figures S1 and S2.

which has reduced peroxisomal activity due to the depletion of *Pex5* (Figure S1B).

We selected 89 genes that exhibited significant differential gene expression between the PG of esg^{GFP}>*Pex5*-i and esg^{GFP}>w^{1118} flies (Table S1) and had known linkage to peroxisomal associated processes, such as response to redox[51] and cytoskeleton remodeling,[52] or exhibited a highly PG-specific expression pattern as reported on Flygut-*seq*[53] but have not been fully functionally characterized or have no known function in intestinal PG maintenance or proliferation (Table S1).

Among genes validated to be differentially expressed in male and female esg^{GFP}>*Pex5*-i compared to sex- and age-matched esg^{GFP}>w^{1118} guts was the gene *ERp60*. Quantitative real-time PCR (RT-qPCR) analyses showed upregulation of *ERp60* in esg^{GFP}>*Pex5*-i compared to esg^{GFP}>w^{1118} midguts (Figures 1D and 1E) in agreement with our transcriptomic results (Figure S1C).

To test if *ERp60* was associated with the increase in PG number observed in esg^{GFP}>*Pex5*-i (Figures 1A–1C), we assessed PG cell number upon *ERp60* overexpression or depletion by two different RNAi lines (Figures S1D, S1F, and S1G). We used the conditional esg^{GFP} driver to express dsRNA targeting *ERp60* or to overexpress *ERp60* cDNA. Conditional expression was initiated from the larval stage onward, and the number of GFP-positive PG cells in the midgut regions of 10-day-old male and female flies was analyzed by fluorescence microscopy. The age was determined based on when an increase in PG numbers was detected in esg^{GFP}>*Pex5*-i flies. Analysis of the posterior midgut regions showed that overexpression of *ERp60* led to an increase in PG in both males and females (Figures 1F–1H). On the other end, RNAi-mediated depletion of ERp60 using two independent RNA lines led to a reduction of PG in the posterior midguts of male and female flies compared to age-matched esg^{GFP}>w^{1118} control flies (Figures 1F–1H). In conclusion, we confirmed that the *ERp60* gene is upregulated in PG with nonfunctional peroxisomes, and genetic manipulation of *ERp60* suggested that it regulates PG number in the posterior midguts of male and female adult flies.

Depletion of *Pex5* in progenitor cells leads to the upregulation of ER-stress response

To understand which cellular processes were associated with ERp60 and the increase in midgut PG number in esg^{GFP}>*Pex5*-i flies, we analyzed our transcriptomic data using gene set enrichment analysis (GSEA) and Cytoscape.[54] This analysis highlighted changes in cellular processes previously reported to be altered in tissues with dysfunctional peroxisomes in *Drosophila*[52] and mammals,[55,56] including changes in carbohydrate and mitochondrial metabolism, responses to oxidative stress, lipids catabolism (e.g., peroxisomal β-oxidation), sphingolipid metabolic processes, and processes of glycerolipid and glycerophospholipid catabolism (Figure S2; Table S1), confirming the reliability of our screen. Additionally, the most differentially expressed genes in esg^{GFP}>*Pex5*-i versus esg^{GFP}>w^{1118} were involved in cytoskeleton regulation and immune signaling, both processes known to be regulated by peroxisome metabolism[29,52,57] (Figure S2). In agreement with the increase in PG number observed in esg^{GFP}>*Pex5*-i, we found the enrichment and clustering of the topmost differentially expressed genes belonged to processes of cell division, stem cell maintenance, and regulation of various signaling pathways that have established roles in PG maintenance, division, and differentiation such as Jak/Stat pathway, EGFR signaling, Wingless, Hpo, and Notch pathways[5,10,58,59] (Figure S2; Table S1).

Our GSEA and Cytoscape transcriptomic analyses also identified ER stress response as a significantly enriched process in esg^{GFP}>*Pex5*-i PG (Figures 1I, 1J, and S2). This included the endoplasmic-reticulum-associated degradation (ERAD) pathway[60] and cellular response to unfolded protein (UPR)[61] (Figures 1I, 1J, and S2; Table S1).

It was reported that defects in peroxisome biogenesis could trigger ER stress through the PERK-eIF2α branch of the UPR.[43,62] What remains unknown is whether other branches of the UPR respond to peroxisomal dysfunction, how peroxisome dysfunction prompts the UPR, and how UPR signaling regulates intestinal stem cell identity, differentiation, and tissue homeostasis.[37,38,63] The marked involvement of these processes in PG increase in response to dysfunctional peroxisomes was notable as *ERp60* encodes a protein disulfide-isomerase ortholog of the human PDIA3 (protein disulfide isomerase family A member 3) involved in protein folding and response to endoplasmic reticulum stress and part of the UPR.[45,64]

Since we found that ERp60, a target of the transcription factor Xbp-1 of the UPR pathway, is upregulated in esg^{GFP}>*Pex5*-i in midguts from male and female adult flies (Figures 1D, 1E, and S1C) and ERp60 overexpression in PG using the esg^{GFP} driver in control flies (Figure S1D) increased the number of midgut PG (Figures 1F–1H), we decided to investigate further how ERp60 controls PG numbers in the posterior midgut.

ERp60 controls PG proliferation but does not impact differentiation in esg^{GFP}>*Pex5*-i posterior midguts

To confirm that the elevated expression of ERp60 observed during the PG peroxisome deficiency of esg^{GFP}>*Pex5*-i flies is associated with the increased midgut PG number of these flies, we genetically depleted ERp60 transcript in esg^{GFP}>*Pex5*-i flies. Fluorescent microscopic analysis showed that ERp60 depletion significantly reduces PG number in esg^{GFP}>*Pex5*-i midguts to the level observed in esg^{GFP}>w^{1118} posterior midguts (Figures 1F–1H and S1H). These findings show that the change in PG number correlates to changes in ERp60 or Pex5 transcript in the analyzed genotypes. Interestingly, we found that depletion of Pex5 in enterocytes using the driver MexGal4[65] did not show induction of *ERp60* (Figure S1E), suggesting that this might be a PG-specific response to peroxisomal dysfunction.

To determine if ERp60 control of PG number occurs during development or also during adult stage, we used the conditional temperature-sensitive Gal4 activation of the esg^{GFP} driver line and performed gene manipulations in PG by shifting the esg^{GFP}>*Pex5*-i, esg^{GFP}>*ERp60*-i or esg^{GFP}>$ERp60^{OE}$ to the permissive temperature after eclosion. We found that the number of PG cells increased in esg^{GFP}>w^{1118} guts when the flies were shifted from 18°C to 29°C and stayed high up to 14 days after the transfer (Figure S1I). Additionally, PG numbers were significantly higher in esg^{GFP}>*Pex5*-i or esg^{GFP}>$ERp60^{OE}$ when adult flies were shifted to 29°C at eclosion and dissected after 14 days but were reduced

considerably in 14-day-old midguts of esg^{GFP}>*ERp60*-i compared with 3-day-old esg^{GFP}>*ERp60*-i and compared to the number observed in the midguts of esg^{GFP}>w^{1118} kept at 29°C for 14 days (Figures S1I–S1L).

We performed immunofluorescence (IF) experiments followed by confocal microscopy analyses to evaluate whether the change in PG cell number observed in esg^{GFP}>*Pex5*-i, esg^{GFP}>*ERp60*-i, and esg^{GFP}>$ERp60^{OE}$ compared to esg^{GFP}>w^{1118} posterior midguts was caused by changes in proliferation or death rate and whether it affected differentiation. Indirect IF studies showed an increase in the number of cells positive for the proliferative marker P-H3[37] in esg^{GFP}>*Pex5*-i (as previously reported[29]) and esg^{GFP}>$ERp60^{OE}$ (Figure S3A) compared with what observed in esg^{GFP}>w^{1118} and esg^{GFP}>*ERp60*-i posterior midguts. On the other hand, indirect IF using the terminal deoxynucleotidyl transferase dUTP nick end labeling (TUNEL) staining to detect apoptosis revealed a higher level of cell death in esg^{GFP}>*ERp60*-i compared to esg^{GFP}>w^{1118}, esg^{GFP}>$ERp60^{OE}$, and esg^{GFP}>*Pex5*-i midguts (Figure S3B). Additionally, we found a reduction in total cell number in the posterior midgut of 14-day-old esg^{GFP}>*ERp60*-i compared with esg^{GFP}>w^{1118}, esg^{GFP}>$ERp60^{OE}$, and esg^{GFP}>*Pex5*-i (Figure S3C).

Upon cell division, each ISC produces a daughter cell that retains the ISC fate and a postmitotic EB that differentiates into either an absorptive enterocyte, EC, or a secretory enteroendocrine cell, EE.[5] Prospero is a homeodomain protein specifically expressed in gut EEs.[12] We observed no change in the number of Prospero-expressing EEs over total number of cells in esg^{GFP}>*ERp60*-i, esg^{GFP}>$ERp60^{OE}$, and esg^{GFP}>*Pex5*-i compared with control esg^{GFP}>w^{1118} midguts (Figure S3D). We concluded that ERp60 controls PG number and is upregulated in response to peroxisome dysfunction, leading to an increase in proliferation in the posterior midguts in a sex-independent manner. This increase in PG does not correlate with a change in differentiation.

Defects in peroxisomal ether lipid metabolism induced overexpression of ERp60 and increase of PG

To determine which branch of peroxisomal metabolism triggers the ERp60-mediated increase in PG, we probed the major peroxisomal metabolic pathways using RNAi to deplete key enzymes of the VLCFA β-oxidation (peroxisomal acyl-coenzyme A oxidase, Acox1), ether lipids synthesis (glyceronephosphate O-acyltransferase, GNPAT), and redox clearance (Catalase, Cat) (Figure S1M) and measure ERp60 transcript. We found an upregulation of ERp60 in the midgut of both esg^{GFP}>*Acox1*-i and esg^{GFP}>*GNPAT*-i flies relative to esg^{GFP}>w^{1118} (Figures 2A and 2B).

On the other hand, although biochemical measurements of hydroxide peroxide (H_2O_2) concentration showed an increase of H_2O_2 in esg^{GFP}>*Cat*-i and esg^{GFP}>*Pex5*-i midguts compared with esg^{GFP}>w^{1118} (Figure S4A), the ERp60 transcript level did not change in esg^{GFP}>*Cat*-i compared with esg^{GFP}>w^{1118} (Figure 2C). Thus, redox stress does not lead to the induction of ERp60. Fluorescent microscopic analyses of the midguts of male and female esg^{GFP}>*Acox1*-i and esg^{GFP}>*GNPAT*-i posterior midguts exhibited an increase in PG cells compared with esg^{GFP}>w^{1118} midguts in correlation with ERP60 overexpression (Figures 2D–2H).

Defects in peroxisomal VLCFA β-oxidation cause accumulation of free fatty acids (FFAs) in cells[66] and tissues.[67] A high-fat diet (HFD) affects the metabolism of flies.[68] It leads to the accumulation of excess FFAs, similar to what is found in tissue with peroxisome defects.[29,67] FFAs are absorbed by the midguts, transformed into neutral storage lipids such as triacyl glycerides, and stored in lipid droplets throughout the midgut, with enrichment found in sections of the anterior and posterior midgut regions.[69] We tested the effect of HFD on ERp60 expression in adult flies fed an HFD enriched with VLCFs to mimic defects in peroxisomal β-oxidation. We compared these flies with flies fed on a balanced cornmeal diet (CMD). Microscopy data revealed that although we observed an increase in PG in both male and female esg^{GFP}>w^{1118} (Figures 2I–2K) and accumulation of lipid droplets in the posterior midguts of HFD-fed flies (Figures S4B and S4C), RT-qPCR analyses did not detect an upregulation of ERp60 in esg^{GFP}>w^{1118} fed on HFD versus CMD (Figure S1D). These data suggest that ERp60-mediated signaling in PG does not respond to FFA lipid stress but is specifically activated in response to dysfunction in peroxisomal lipid metabolism. We treated the flies with niacin (vitamin B3), which has been shown to reduce the amount of FFA in mammals[29,66,70,71] and *Drosophila*,[52] a part having anti-oxidant effects.[72,73] Biochemical analyses showed that treatment with niacin was able to lower the amount of FFAs and H_2O_2 in esg^{GFP}>*Pex5*-i midguts to control levels, confirming his lipid scavenger and anti-oxidant activity in *Drosophila* guts[52,66] (Figures S4A and S4E). However, fluorescent microscopy analyses of esg^{GFP}>w^{1118} and esg^{GFP}>*Pex5*-i midguts showed that treatment with niacin did not reduce PG number in esg^{GFP}>*Pex5*-i to numbers comparable to what was observed in esg^{GFP}>*Pex5*-i midguts in both males and females (Figures S4F and S4G). Additionally, microscopy analyses showed that esg^{GFP}>*ERp60*-i fed HFD did not increase PG number in the posterior midguts compared to esg^{GFP}>*ERp60*-i fed on CMD, confirming that ERp60 does not respond to VLCFA lipotoxic stress caused by dysfunction in peroxisomal β-oxidation (Figures S4H and S4I).

Together, these results confirmed that accumulation in VLCF or redox species caused by defects in peroxisomal β-oxidation or anti-oxidant activities do not trigger the increase in PG number observed in esg^{GFP}>*Pex5*-i midguts.

The first step in *de novo* ether lipid synthesis is mediated by the peroxisomal enzyme glycerophosphate O-acyltransferase (GNPAT), which has a strict substrate specificity reacting only with the long-chain acyl-CoAs that can be imported from the cytosol or produced intraperoxisomal by chain shortening of CoA esters of VLCFA peroxisomal β-oxidation.[74] AGPS subsequently catalyzes the substitution of the acyl chain with a long-chain fatty alcohol, resulting in the formation of alkyl-DHAP and the release of the fatty acid that is subsequently transported to the ER, where the final steps of ether lipid synthesis occur.[75] Since we observed an increase in PG in the midguts of flies with metabolic ablation of the VLCFAs β-oxidation (esg^{GFP}>*Acox1*-i) guts and ether phospholipid pathways (esg^{GFP}>*GNPAT*-i), we probed whether the reduction in ether phospholipids specifically triggers PG increase in esg^{GFP}>*Pex5*-i. GNPAT catalyzes the conversion of dihydroxyacetone

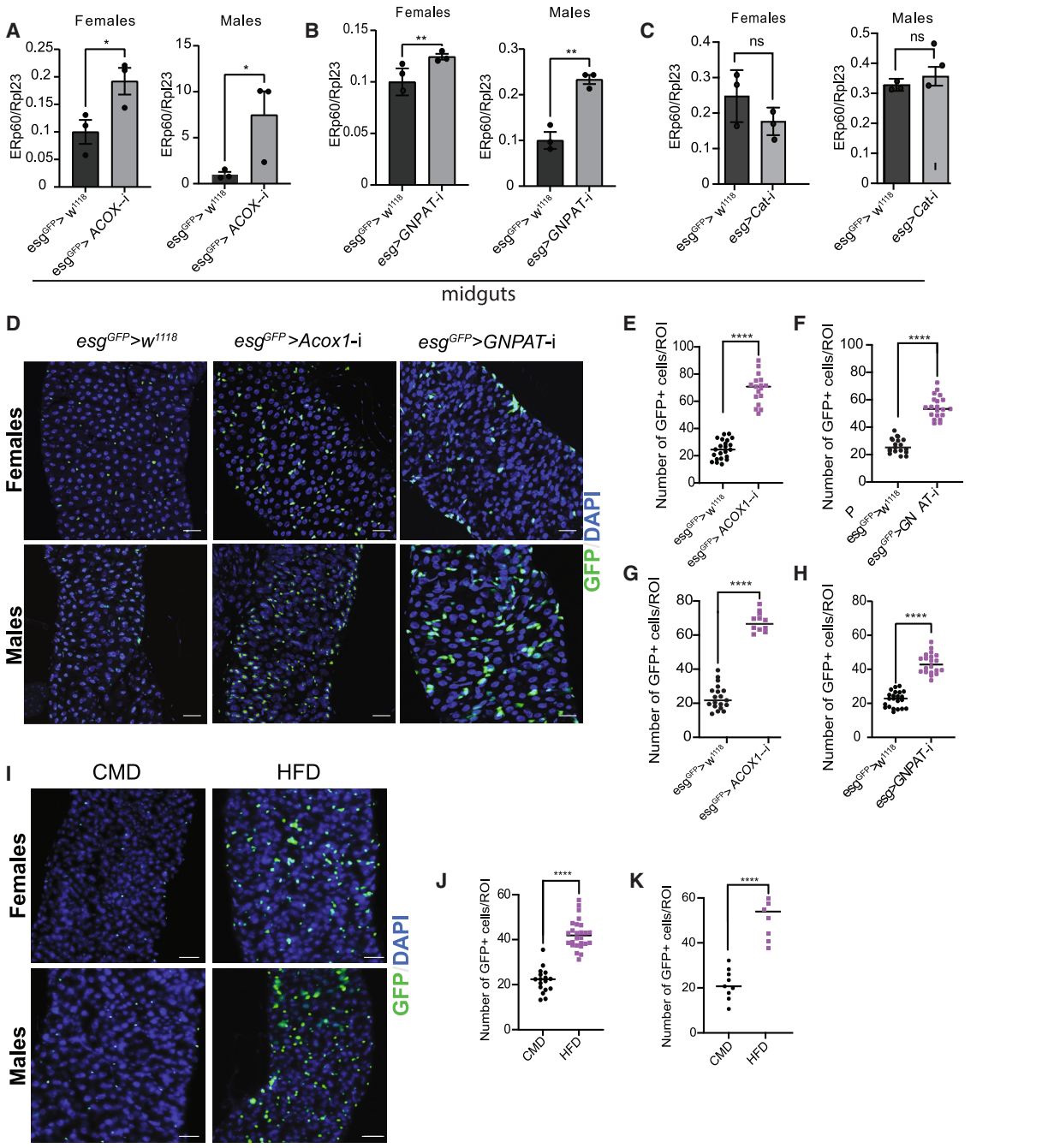

Figure 2. Deregulation of peroxisomal lipid metabolism triggers ERp60 upregulation in esg-positive cells and affects progenitors' number

(A–C) The bar graphs show the ERp60 amount in the midguts of adult female (left) or male (right) flies of the reported genotypes. $n = 3$.

(D) Fluorescent microscopic analyses of esg^{GFP}-positive cells in adult posterior midguts from female (upper panels) or male (lower panels) flies of the reported genotypes. Scale bar, 10 μm.

(E–H) The dot plots represent the number of esg^{GFP}-positive cells per ROI in adult posterior midguts of female (upper panels) *esg^{GFP}>w^{1118}* and *esg^{GFP}>ACOX1*-i (E) and *esg^{GFP}>w^{1118}* and *esg^{GFP}>GNPAT*-i (F) or male (lower panels) *esg^{GFP}>w^{1118}* and *esg^{GFP}>ACOX1*-i (G) and *esg^{GFP}>w^{1118}* and *esg^{GFP}>GNPAT*-i (H). $n = 15–20$.

(I) Representative images of fluorescent microscopy analyses indicating esg^{GFP}-positive cells in posterior midgut regions of female (upper panels) or male (lower panels) *esg^{GFP}>w^{1118}* control flies fed a balanced cornmeal diet (CMD) or a cornmeal diet supplemented with 20% added fats (HFD; 4:1 coconut oil versus broccoli oil). Scale bar, 20 μm. The dot plots represent the number of esg^{GFP}-positive cells per ROI in adult posterior midguts of female (J) or male (K) *esg^{GFP}>w^{1118}* flies fed CMD or HFD. n = 5–30. In every image the DNA was stained by DAPI (blue). The error bars in (A–C), (E–H), and (J and K) represent the standard deviation of the mean. Statistical significance was calculated using unpaired t tests. ****$p < 0.0001$; **$p < 0.01$; *$p < 0.05$; ns, not significant. See also Figures S1 and S4.

phosphate (DHAP) and acyl-CoA into acyl-DHAP and CoA. We supplemented the diet of 3-day-old esgGFP>w1118 and esg^{GFP}>*Pex5*-i flies with an alkyl-DHAP, 1-*O*-Octadecyl-rac-glycerol (batyl alcohol) for 4 days, and then we dissect the guts and performed fluorescent microscopy analyses. Batyl alcohol could rescue PG number in esg^{GFP}>*Pex5*-i midguts to the number observed in esg^{GFP}>w^{1118} midguts (Figures S5A and S5B). Interestingly, adding batyl alcohol to the diet of esg^{GFP}>w^{1118} and esg^{GFP}>$ERp60^{OE}$did not impact PG number (Figures S5A and S5B). These data suggest that ERp60 acts downstream of plasmalogen synthesis.

Lipidomic analyses of esg^{GFP}>*Pex5*-i midguts showed that the amount of ether-phosphatidylethanolamine (PE) and ether-phosphatidylcholine (PC) that are produced by peroxisomes and can affect the total level of PE and PC were reduced in esg^{GFP}>*Pex5*-i midguts compared with control midguts (Figures S5C and S5D).[33] We also found that levels of PE and PC core phospholipids, which are essential for membrane functions and that are affected by peroxisomal ether lipids synthesis, were reduced in esg^{GFP}>*Pex5*-i midguts compared with esg^{GFP}>w^{1118} midguts[76] (Figures S5E and S5F). We measured the ratio of PC:PE, which is essential for biological membrane function, including the ER membranes,[77] and their ratio was impacted (Figure S5G). Alteration of lipid composition in the membrane has been shown to activate the UPR.[78–81] Abnormally high and low cellular PC/PE ratios were linked to misfolding of membrane proteins and alteration of cellular signaling.[77,82,83] In conclusion, alteration in peroxisomal ether-phospholipid synthesis appeared to cause changes in cellular amounts of major lipids. This might explain the ER stress response activation detected by the transcriptomic results and the increase in PG number in esg^{GFP}>*Pex5*-i.

ERp60 regulates intestinal stem cell number and controls tissue size

The *Drosophila* ERp60 is the orthologous of human PDIA3. PDIA3 is known to be localized mainly at the ER, where it participates in correcting the folding of glycoprotein that needs to be localized to the plasma membrane or secreted. PDIA3 is activated by various stresses (e.g., oxidative, metabolic), and it is also known to be a transcriptional target of Xbp-1 of the UPR in response to ER stress.[44] PDIA3 was reported to regulate various cellular processes, including cell growth and death and cell division, and plays a role in cytokine-dependent signal transduction.[46–48]

To elucidate the role of ERp60 in PG regulation and intestinal regeneration, we performed microscopy analyses of intestines dissected from 3- or 14-day-old esg^{GFP}>w^{1118} and esg^{GFP}>*ERp60*-i flies where the system was activated from L1 stage.

We found that in 3-day-old flies, the esg^{GFP}>*ERp60*-i intestines were about the same size as age-matched esg^{GFP}>w^{1118} (Figure 3A). On the other hand, esg^{GFP}>*ERp60*-i intestines were about three times smaller than age-matched esg^{GFP}>w^{1118} in 14-day-old flies (Figure 3B), in agreement with a significant reduction in PG number (Figures 1F–1H). We reported that when the RNAi was activated at L1, we observed a reduction of PG number in posterior midguts of 3-day-old adult esg^{GFP}>*ERp60*-i (Figures 1F–1H). Indirect IF experiments using TUNEL staining to detect apoptosis revealed a higher level of cell death in esg^{GFP}>*ERp60*-i compared to esg^{GFP}>w^{1118} and esg^{GFP}>*Pex5*-i midguts (Figures 3C and 3D) already at day 3 post-eclosion, before intestinal size was impacted. Moreover, immunofluorescence analyses of midguts stained with the ISC marker Delta indicated a loss of ISC and EB in esg^{GFP}>*ERp60*-i midguts (Figures 3E–3H), suggesting that ERp60 has a role in both stem cell and EB survival.

Stem cell proliferation is regulated by ERp60 downstream of the Xbp1 branch of UPR and activated by ER stress response

ERp60 is one of the genes induced by the UPR activated in response to ER stress. Three highly conserved UPR sensors coordinate the cell-autonomous response to ER stress: PERK, the transcription factor ATF6, and the endoribonuclease IRE1. IRE1 promotes splicing of the mRNA encoding the transcription factor Xbp1, PERK phosphorylates and inhibits the translation initiation factor 2 alpha (eIF2α),[37,38,84–86] and ER-stress-induced cleavage of ATF6 promotes its nuclear translocation and activation of stress response genes. The activation of Xbp1 and ATF6 results in transcriptional induction of ER chaperones, of genes encoding ER components, and of factors required to fold or degrade un/misfolded proteins, thus enhancing ER folding capacity.[37,87]

ER stress and UPR are significantly enriched in the list of the utmost differentially expressed genes in PG of esg^{GFP}>*Pex5*-i compared to esg^{GFP}>w^{1118}, and ERp60 is a target of Xbp1 and contributes to the proteostatic tolerance of the UPR response.[44] We wanted to validate which branch of the UPR was activated in esg^{GFP}>*Pex5*-i and whether its activation caused the ERp60-induced increase in PG number in esg^{GFP}>*Pex5*-i. To do this, we probed the activation of the IRE1-Xbp1 branch of the UPR. IRE1 activation in response to ER stress promotes an unconventional splicing of the Xbp1 transcript. Xbp1 has a 23-nucleotide intron that is removed from the transcript upon activation of IRE1. We performed RT-PCR using primers that surround the 23-nucleotide intron region to probe for Xbp1 splicing, measuring the amount of Xbp1 mRNA full length (240 base pairs amplicon) or a short form (220 bp amplicon) in esg^{GFP}>w^{1118} and esg^{GFP}>*Pex5*-i midguts. We could detect a strong signal for the Xbp1 240 bp amplicon and a weak signal for the 220 bp amplicon in esg^{GFP}>w^{1118} samples conversely; we observed a fainter 240 and a stronger 220 bp amplicon in esg^{GFP}>*Pex5*-i total RNA and esg^{GFP}>w^{1118} midgut total RNA extracted from dehydrated flies (Figures 4A–4C) that acted as a positive control of ER stress.

To detect the activation of the ATF6 branch of the UPR, an increase in the ATF6 transcript level is a reliable readout.[32] We measured ATF6 transcript level in esg^{GFP}>*Pex5*-i compared to esg^{GFP}>w^{1118} midguts. RT-qPCR analyses did not identify any significant change in ATF6 transcript level in the midguts of the analyzed genotypes (Figure S6A), suggesting this branch of the UPR was not activated in PG due to peroxisome dysfunction.

The other branch of the UPR, PERK-eIF2α, induces inhibition of global translation, and its activation was found to regulate intestinal homeostasis in *Drosophila*.[37] We probed whether this branch of the UPR was active in esg^{GFP}>*Pex5*-i midguts. We performed indirect immunofluorescent studies to investigate the activation of eIF2 α, measured by the amount of phosphorylated

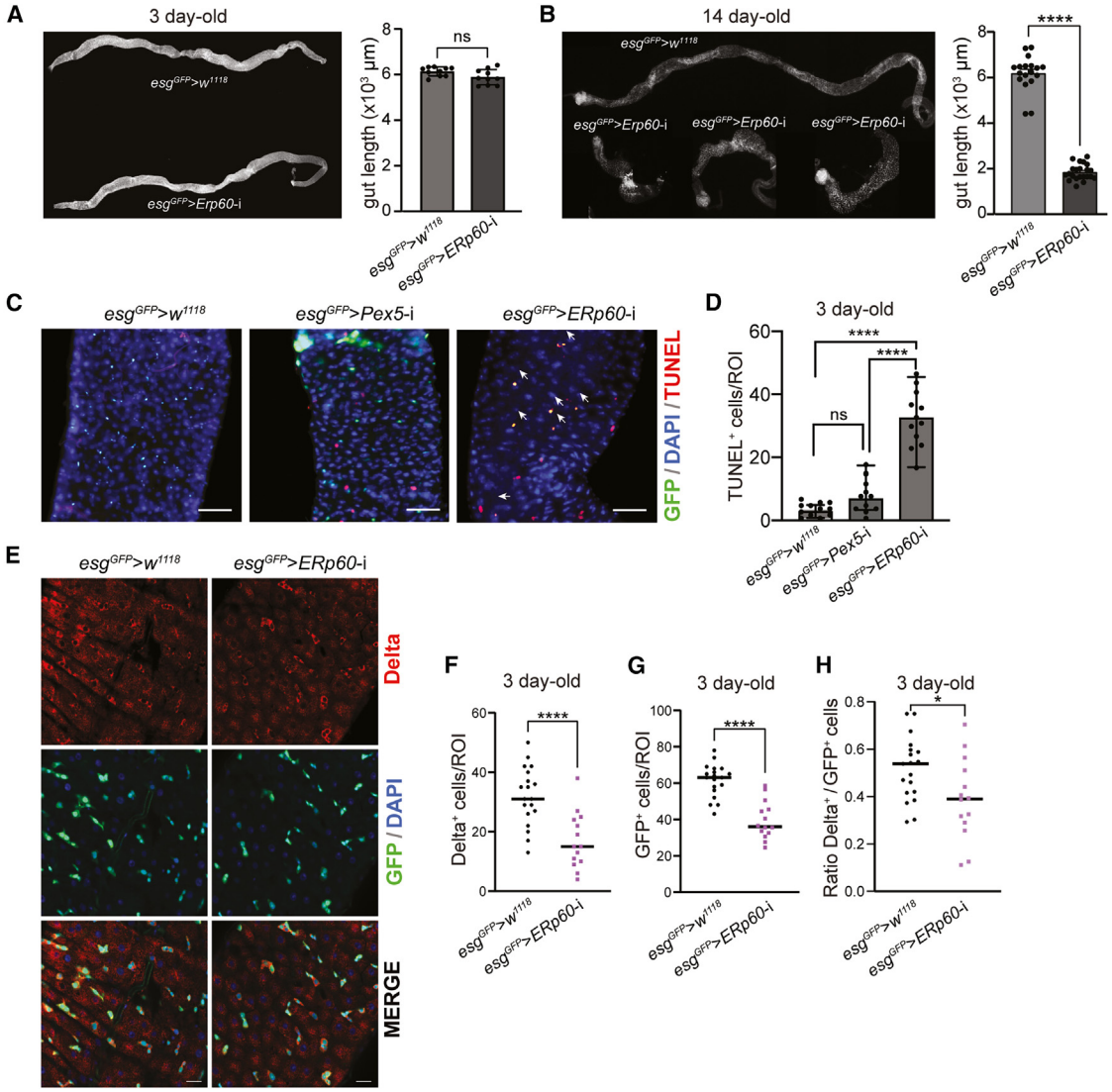

Figure 3. Deficiency in ether lipids metabolism increases progenitor numbers in *esg^{GFP}>Pex5*-i midguts

(A) Image showing the side-by-side comparison of the length of the intestine of adult *esg^{GFP}>w^{1118}* versus *esg^{GFP}>ERp60*-i 3-day-old flies. Scale bar, 50 μm. The graph bar reports the mean value of gut length in *esg^{GFP}>w^{1118}* and *esg^{GFP}>ERp60*-i flies. *n* = 20.

(B) Image showing the side-by-side comparison of the length of the intestine of adult *esg^{GFP}>w^{1118}* versus *esg^{GFP}>ERp60*-i 14-day-old flies. Scale bar, 50 μm. The graph bar reports the mean value of gut length in *esg^{GFP}>w^{1118}* and *esg^{GFP}>ERp60*-i flies. *n* = 20.

(C) Fluorescent microscopic images indicating the esg^{GFP}-cells (green) and TUNEL (red) in posterior midguts of *esg^{GFP}>w^{1118}*, *esg^{GFP}>Pex5*-i, and *esg^{GFP}>ERp60*-i flies. Scale bar, 20 μm. Arrowheads indicate the esg^{GFP} TUNEL double-positive cells.

(D) The graph bar reports the number of esg^{GFP}-cells per ROI in *esg^{GFP}>w^{1118}*, *esg^{GFP}>Pex5*-i, and *esg^{GFP}>ERp60*-i posterior midguts. *n* = 10.

(E) Representative indirect immunofluorescent image indicating a reduction of Delta^{+} cells and esg^{GFP} cells in posterior midgut regions of *esg^{GFP}>w^{1118}* and *esg^{GFP}>ERp60*-i flies. Scale bar, 20 μm.

(F–H) The dot plots represent the number of Delta^{+} cells (F), esg^{GFP} (G), and the ratio between Delta^{+} cells and esg^{GFP} (H) per ROI in *esg^{GFP}>w^{1118}* and *esg^{GFP}>ERp60*-i posterior midguts. *n* = 11–17. In every image the DNA was stained by DAPI (blue). The error bars represent the standard deviation of the mean. Statistical significance in (C) was calculated using a one-way ANOVA test and in (A), (B), and (F–H) calculated using unpaired t tests. ****$p < 0.0001$; **$p < 0.01$; *$p < 0.05$; ns, not significant. See also Figure S4.

protein at serin 51. Confocal microscopy analyses showed an increase in P-eIF2 α in *esgGFP>Pex5*-i compared with what was observed in *esg^{GFP}>w^{1118}* midguts (Figures 4D and 4E). These data are in agreement with the downregulation of ribosomal genes detected in the transcriptomic analyses (Figure S2) that indicated reduced protein synthesis.

As eIF2α represents a convergence point of different stress pathways,[88] we checked the involvement of PERK-eIF2α signaling branch in the increase in PG of *esg^{GFP}>Pex5*-i midguts by probing the PERK's participation in driving the rise in PG of *esg^{GFP}>Pex5*-i midguts. We performed genetic interaction by introducing in *esg^{GFP}>Pex5*-i the PERK mutant allele

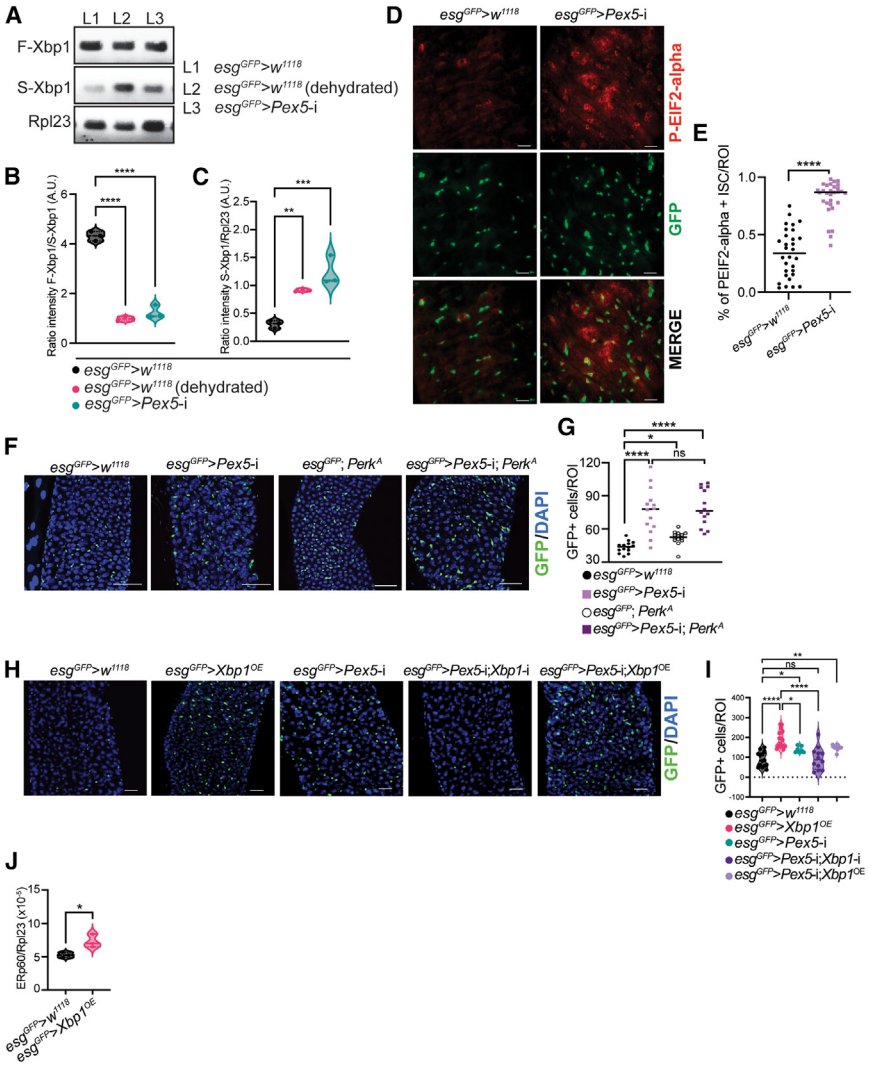

Figure 4. Defects in peroxisomal metabolism in progenitor cells activate the EIF2α/Xbp1/ERp60 branch of the UPR and increase progenitors

(A) Representative agarose gel image showing amplicons detecting unspliced and spliced Xbp1 transcript. The representative gel indicates a decrease in full-length Xbp1 transcript and an increase in the short-spliced variant of Xbp1 in dehydrated (stressed) $esg^{GFP}>w^{1118}$ and $esg^{GFP}>$ *Pex5*-i compared with $esg^{GFP}>w^{1118}$.

(B and C) The violin plots report the value of the ratio metric analyses between Xbp1 full-length versus Xbp1 spliced variant (B) and the ratio values of the band intensity of Xbp1 spliced variant versus Rpl23 (C) in the midguts of $esg^{GFP}>w^{1118}$, dehydrated $esg^{GFP}>w^{1118}$, and $esg^{GFP}>$*Pex5*-i flies. $n = 3$.

(D) Indirect immunofluorescence images showing P-EIF2-α (red) and esg^{GFP} cells (green) in posterior midguts of adult $esg^{GFP}>w^{1118}$ and $esg^{GFP}>$*Pex5*-i flies. Scale bar, 25 μm.

(E) The dot plot represents the number of esg^{GFP}-cells per ROI in the adult posterior midguts of the indicated genotypes. $n = 25–30$.

(F) Representative immunofluorescent images indicating esg^{GFP}-cells (green) in posterior midguts of $esg^{GFP}>w^{1118}$, $esg^{GFP}>$*Pex5*-i, $Perk^{A}$ and $esg^{GFP}>$*Pex5*-i; $Perk^{A}$ flies. Scale bar, 25 μm.

(G) The dot plot represents the number of esg^{GFP} cells per ROI in the adult posterior midguts of the indicated genotypes. $n = 10–35$.

(H) Representative immunofluorescent images indicating esg^{GFP} cells (green) in posterior midguts of $esg^{GFP}>w^{1118}$, $esg^{GFP}>Xbp1^{OE}$, $esg^{GFP}>$*Pex5-i*, $esg^{GFP}>$*Xbp1-i*; *Pex5*-i and *esgGFP>Pex5-i; Xbp1*^{OE} Scale bar, 25 μm.

(I) The violin plot represents the number of esg^{GFP}-cells per ROI in the adult posterior midguts of the indicated genotypes. n = 7–10.

(J) The violin plot reports the relative gene expression of ERP60 in midguts of $esg^{GFP}>w^{1118}$ and $esg^{GFP}>Xbp1^{OE}$. $n = 3$. In every image the DNA was stained by DAPI (blue). The error bars represent the standard deviation of the mean. Statistical significance in (E and J) was calculated using unpaired t tests. In contrast, statistical significance in (B, C, G, and I) was calculated using a one-way ANOVA test. $^{**}p < 0.01$, $^{*}p < 0.05$; ns, not significant. See also Figures S5 and S6.

PERK$^{\Delta}$ to reduce its activity. Fluorescent microscopy analyses indicated that PERK$^{\Delta}$ heterozygous flies present a higher number of PG in the midguts, although significantly lower than the number observed in $esg^{GFP}>$*Pex5*-i midguts. However, PERK$^{\Delta}$ allele in $esg^{GFP}>$*Pex5*-i genetic background did not reduce the number of PG observed in $esg^{GFP}>$*Pex5*-i midguts (Figures 4F and 4G). Since eIF2α phosphorylation in ISCs of tunicamycin-treated flies is associated with increased Xbp1 splicing,[89,90] we concluded that activation of eIF2α might be independent of PERK and converging into the IRE-Xbp1 signaling.

To confirm that the increase in PG number in $esg^{GFP}>$*Pex5*-i midguts is caused by the Xbp1 branch of UPR, which promotes the upregulation of ERp60, we overexpressed the spliced variant of Xbp1 in PG cells. Fluorescent microscopy data revealed an increase in PG cells in $esg^{GFP}>Xbp1^{OE}$ compared to what was observed in control $esg^{GFP}>w^{1118}$ midguts (Figures 4H and 4I), and this correlated with higher ERp60 transcript amount in $esg^{GFP}>Xbp1^{OE}$ compared with control $esg^{GFP}>w^{1118}$ midguts (Figure 4J). Interestingly, genetic depletion of Xbp1 in PG of $esg^{GFP}>$*Pex5*-i midguts showed a rescue in PG number close to the level observed in $esg^{GFP}>w^{1118}$ midguts (Figures 4H and 4I).

Finally, we probed for mitochondrial stress response by measuring the transcript levels of genes that encode proteins involved in mitophagy (*Pink1*),[91] mitochondrial heat shock proteins (such as hsp22, hsp60c, hsc70),[92] and genes that encode for proteins that are core metabolic regulators that respond to mitochondrial stress, such as *Sirt1*[93,94] and *hnf4*.[95,96]

RT-qPCR analyses did not measure significant changes in these transcripts in the midguts of the analyzed genotypes (Figures S6B–S6D). Together, these data show that ERp60 controls intestinal regeneration and is triggered by activation of the Xbp1 branch of UPR that causes an increase in PG in the midguts under metabolic stress due to defects in peroxisomal ether phospholipid metabolism.

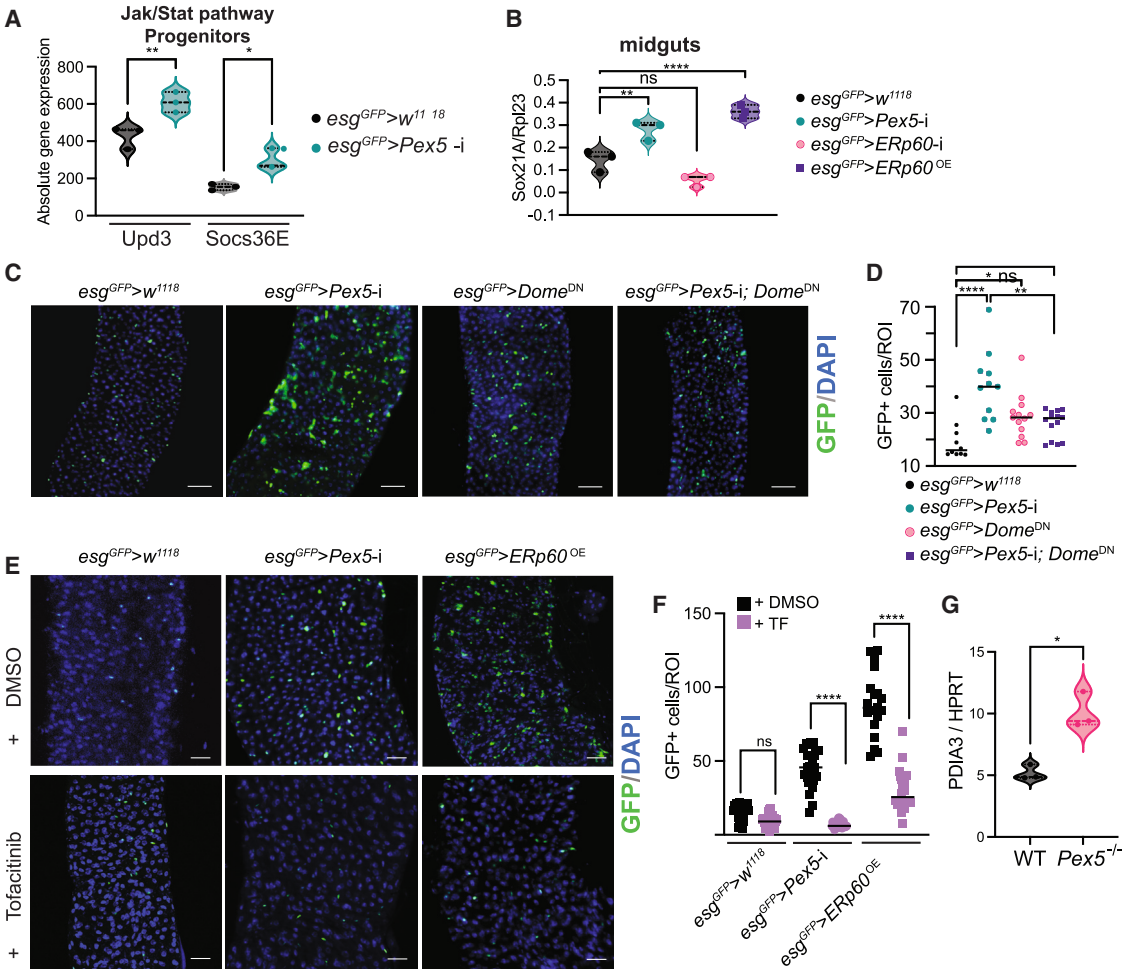

Figure 5. Upregulation of *ERp60* enhances Jak/STAT signaling to increase intestinal progenitor cells in response to peroxisomal metabolic defects

(A) The violin plot indicates the absolute transcript counts detected by the RNAseq analyses for the reported genes in $esg^{GFP}>w^{1118}$ and $esg^{GFP}>Pex5$-i progenitor cells. $n = 3$. (B) The violin plot represents the relative gene expression of Sox21A versus Rpl23 used as an internal control in $esg^{GFP}>w^{1118}$ and $esg^{GFP}>Pex5$-i midguts. $n = 3$. (C) Representative fluorescent images indicating esg^{GFP}-cells in posterior midgut regions of $esg^{GFP}>w^{1118}$, $esg^{GFP}>Pex5$-i, $esg^{GFP}>Dome^{DN}$, and $esg^{GFP}>Pex5$-i; $esg^{GFP}>Dome^{DN}$ flies. Scale bar, 20 μm.

(D) The dot plot indicates the number of esg^{GFP} cells per ROI in the posterior midguts of flies of the reported genotypes. $n = 10$.

(E) Representative fluorescent images indicating esg^{GFP} cells in posterior midgut regions of $esg^{GFP}>w^{1118}$, $esg^{GFP}>Pex5$-i, and $esg^{GFP}>ERp60^{OE}$ fed regular cornmeal food supplied with DMSO (vehicle) or the Jak inhibitor tofacitinib. Scale bar, 20 μm.

(F) The dot plot indicates the number of esg^{GFP} cells per ROI in the posterior midguts of flies of the reported genotypes and under the indicated conditions. $n = 15–20$.

(G) The violin plot represents the relative gene expression of PDIA3 versus HRPT used as an internal control in WT and $Pex5^{-/-}$ murine intestinal organoid cultures. In every image, the DNA was stained with DAPI (blue). The error bars represent the standard deviation of the mean. Statistical significance in (A and G) was calculated using an unpaired t test, statistical significance in (B and D) was calculated using a one-way ANOVA test, and the statistical significance in (F) was computed using a two-way ANOVA test. $^{****}p < 0.0001$, $^{**}p < 0.01$, $^{*}p < 0.05$; ns, not significant. See also Figures S5 and S6.

The increase of PG number in $esg^{GFP}>Pex5$-i midguts is driven by the Jak/STAT pathway

Multiple signaling controls PG proliferation/differentiation to promote intestinal regeneration in *Drosophila* and mammals. To elucidate the mechanism by which ERp60 triggers PG proliferation in response to metabolic stress in ISC and EB, we searched the transcriptomic data for the expression levels of genes that are established indicators of activation of the major pathways involved in the regulation of PG in *Drosophila* and mammals,[97,98] including the EGF, Wnt, Notch, JAK/STAT, Hpo, and IRs pathways. We looked for the absolute transcript counts in the RNA-seq analysis. We found that targets of EGFR pathway (*pnt*, *cdc25* and *spi*), Wnt (*ftz* and *nkd*), IRs (*thor*), Notch (*Su(h)*), and Hpo (*dIAP1*) were detected in the transcriptomic analyses but were not upregulated in $esg^{GFP}>Pex5$-i compared with $esg^{GFP}>w^{1118}$ PG (Figures S6E–S6G). On the other hand, the target transcript of the Jak/Stat pathway *Socs36E* was upregulated in $esg^{GFP}>Pex5$-i (Figure 5A), suggesting higher activation of Jak/Stat pathway in $esg^{GFP}>Pex5$-i PG (Figure 5A). To confirm it, we performed RT-qPCR experiments to measure the

transcript of another characterized downstream target of Jak/Stat in PG, *Sox21A*, which is known to regulate their proliferation in response to stress or damage.[99] We found that Sox21A transcript is upregulated in *esgGFP>Pex5*-i and $esg^{GFP}>ERp60^{OE}$ midguts compared with its amount in control $esg^{GFP}>w^{1118}$ midguts but is reduced in $esg^{GFP}>ERp60$-i compared with $esg^{GFP}>w^{1118}$, $esg^{GFP}>Pex5$-I, and $esg^{GFP}>ERp60^{OE}$ midguts (Figure 5B).

To confirm that Jak/Stat pathway is the major signaling driving PG increase in $esg^{GFP}>Pex5$-i, we performed genetic and chemical manipulation of the activating upstream receptor known as Dome in *Drosophila*. Dome is activated upon binding to the ligand Upd3. We found that the level of Upd3 was upregulated in $esg^{GFP}>Pex5$-i compared to $esg^{GFP}>w^{1118}$ in PG cells (Figure 5A). However, when we tested the amount of Upd3 transcript in $esg^{GFP}>Pex5$-i midguts compared to $esg^{GFP}>w^{1118}$, we observed no difference, suggesting that the production of Upd3 and activation of the Jak/STAT signal is cell autonomous in $esg^{GFP}>Pex5$-i (Figure S6H). Of note, when we measured the amount of Upd3 mRNA in $esg^{GFP}>ERp60$-i compared with $esg^{GFP}>w^{1118}$ midguts, we recorded a significantly high expression of Upd3 (Figure S6I), suggesting that depletion of ERp60 in PG leads to release of inflammatory and proliferative signaling in the midgut.

We overexpressed the dominant negative allele for *Dome* in PG and observed that $esg^{GFP}>Dome^{DN}$ had a PG number similar to that observed in $esg^{GFP}>w^{1118}$. However, when we overexpressed this allele in $esg^{GFP}>Pex5$-i, we measured a significant reduction in PG number in the midguts of $esg^{GFP}>Pex5$-i; $Dome^{DN}$ (Figures 5C and 5D). We then treated flies with an established inhibitor of Jak, tofacitinib,[100,101] and found a reduction in PG number in *esgGFP>Pex5*-i and $esg^{GFP}>ERp60^{OE}$ similar to what was observed in $esg^{GFP}>w^{1118}$ midguts (Figures 5E and 5F). We concluded that the JAK/STAT pathway mediated the increase in PG proliferation triggered by peroxisomal dysfunction and ERp60 activation in midguts. Of note, in mammals, the ortholog of ERp60, PDIA3, is linked to hepatocellular carcinoma progression,[48] suggesting a connection between PDIA3/ERp60 and proliferative pathways.

Interestingly, RT-qPCR analyses on homozygous mutant $Pex5^{-/-}$-derived murine intestinal organoids show a significant upregulation of PDIA3 compared with its expression in organoids derived from wild-type (WT) small intestines (Figure 5G).

$esg^{GFP}>Pex5$-i and $esg^{GFP}>ERp60^{OE}$ males have compromised barrier function and reduced lifespan

To determine whether the increase in PG found in $esg^{GFP}>Pex5$-i and $esg^{GFP}>ERp60^{OE}$ affects animal physiology, we performed a survival assay of $esg^{GFP}>w^{1118}$, $esg^{GFP}>Pex5$-i, and $esg^{GFP}>ERp60^{OE}$ males and females. We recorded sex-specific results. The $esg^{GFP}>Pex5$-i and $esg^{GFP}>ERp60^{OE}$ males started to die faster than $esg^{GFP}>w^{1118}$ around 12 days post-eclosion, and they continued to die faster, and at 23 and 20 days post-eclosion, respectively, all the flies were dead, whereas 70% of $esg^{GFP}>w^{1118}$ control flies were still alive (Figure 6A). On the contrary, $esg^{GFP}>w^{1118}$, $esg^{GFP}>Pex5$-i, and $esg^{GFP}>ERp60^{OE}$ females presented similar survival rates (Figure 6B). On the note, $esg^{GFP}>Pex5$-*i* seemed to have a higher survival rate when compared with $esg^{GFP}>w^{1118}$ and $esg^{GFP}>ERp60^{OE}$ from day 10–20 post-eclosion; however, this improvement in survival was not statistically significant (Figure 6B). To understand whether the reduction in survival observed in $esg^{GFP}>Pex5$-i and $esg^{GFP}>ERp60^{OE}$ males was caused by damage to the intestinal epithelial barrier, we used the Smurf assay[102] to assess the loss/reduction of intestinal barrier function in $esg^{GFP}>w^{1118}$, $esg^{GFP}>Pex5$-i, and $esg^{GFP}>ERp60^{OE}$ males and females at 20 days post-eclosion. In the assay, the permeability is detected by a nonabsorbable blue food dye outside the digestive tract after feeding, referred to as Smurf.[102,103] Both male and female $esg^{GFP}>w^{1118}$ flies showed blue-colored food retained in the intestine, whereas $esg^{GFP}>Pex5$-i and $esg^{GFP}>ERp60^{OE}$ male flies showed blue dye throughout the abdomen (Figures 6C and 6D). Differently, $esg^{GFP}>Pex5$-i and $esg^{GFP}>ERp60^{OE}$ females showed the blue-colored food retained in the intestine similarly to $esg^{GFP}>w^{1118}$ flies (Figures 6C and 6D). The $esg^{GFP}>w^{1118}$ flies fed for 24 h with sucrose in 2% SDS solution to trigger epithelial barrier damage were used as a positive control for increased permeability and exhibited the blue dye throughout their body (Figure 6D). In conclusion, $esg^{GFP}>Pex5$-i and $esg^{GFP}>ERp60^{OE}$ males were partial "Smurfs," indicating that the barrier function of the intestinal epithelium was compromised in flies with dysfunctional peroxisomes or high expression of ERp60 in the PG. Downregulation of *ERp60* in $esg^{GFP}>Pex5$-i rescued the intestinal barrier function in males compared with $esg^{GFP}>Pex5$-i males but did not impact gut permeability in $esg^{GFP}>Pex5$-i females (Figures 6E and 6F). Additionally, $esg^{GFP}>Pex5$-i; *ERp60*-i males showed a survival rate similar to $esg^{GFP}>w^{1118}$ flies (Figures 6G and 6H). Interestingly, the treatment of $esg^{GFP}>Pex5$-i males with batyl alcohol rescues the epithelial barrier function defects (Figures S7A and S7B) and reduces *ERp60* upregulation in the gut of male and female $esg^{GFP}>Pex5$-i (Figure S7C), correlating PG number to ether lipid cellular amount and barrier function in male flies.

Thus, alteration of peroxisomal ether lipid metabolism and activation of ERp60 as a consequence of Xbp1 signaling of ER stress response in PG compromises intestinal epithelial barrier function in adult male *Drosophila* and affects lifespan. Overall, our study identified a gene important for ISC maintenance and healthy regeneration of the intestinal epithelium in physiological conditions and under lipid-mediated metabolic stress (Figure 7A).

DISCUSSION

The role of metabolism in intestinal homeostasis is emerging as an important area of investigation to identify pathways involved in epithelial regeneration and function[15] and better understand how the already identified signaling[6,7,12] is regulated by metabolic shift.

Metabolism controls cellular function and can produce products that act as signaling molecules regulating various cellular and tissue functions.[15,18,22] Recent studies have highlighted the importance of mitochondrial metabolic pathways in ISC homeostasis,[15] attracting interest in the importance of different organelles and their metabolisms in maintaining intestinal epithelial regeneration.[25] In our study, we define the importance of peroxisome ether phospholipid metabolism in

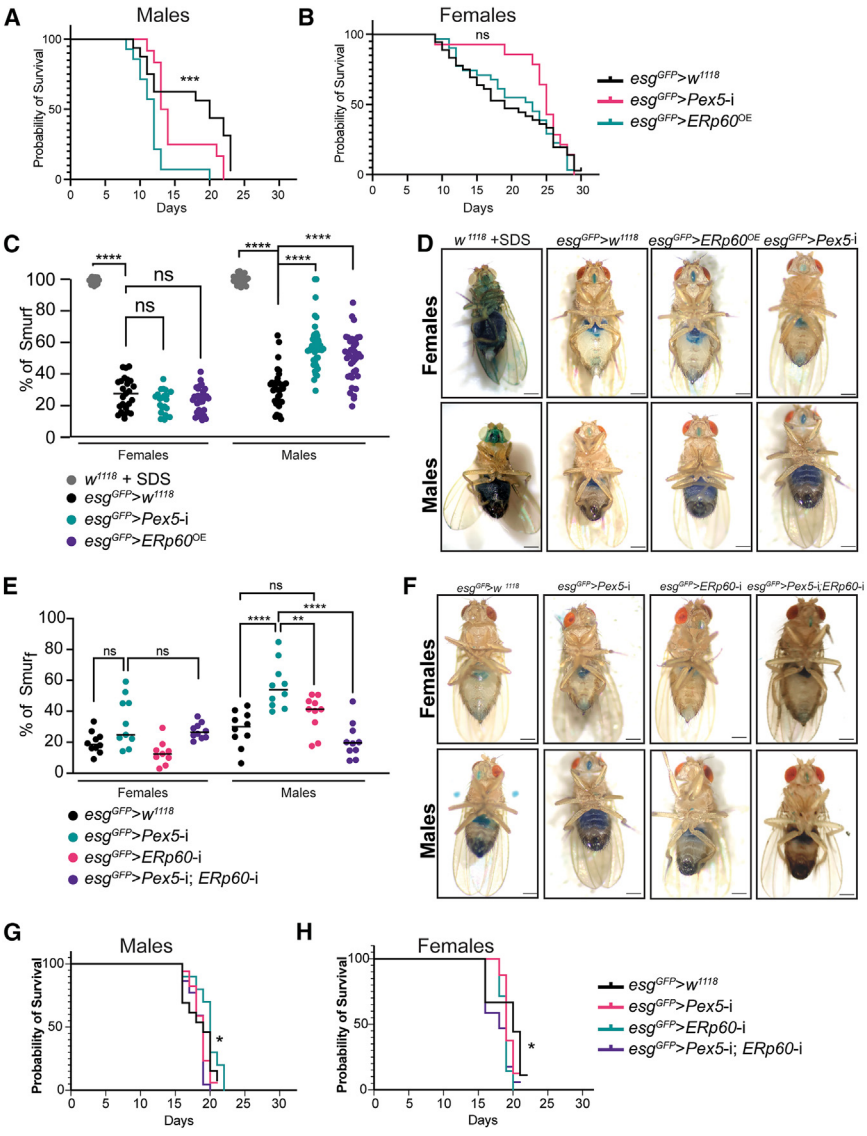

Figure 6. Upregulation of *ERp60* leads to failure in epithelial barrier function and reduces survival in males

(A) Survival of $esg^{GFP}>w^{1118}$, $esg^{GFP}>$*Pex5*-i, and $esg^{GFP}>ERp60^{OE}$ male flies.

(B) Survival of $esg^{GFP}>w^{1118}$, $esg^{GFP}>$*Pex5*-i, and $esg^{GFP}>ERp60^{OE}$ female flies. *n* = 100 flies per genotype.

(C) The bar graph indicates the percentage of dark blue area divided by the total abdomen area. *n* = 20–30 flies per genotype.

(D) Representative picture of the Smurf assay on 20-day-old female (top) or male (bottom) flies. Scale bar, 500 μm.

(E) The bar graph indicates the percentage of dark blue area divided by the total abdomen area. *n* = 10 flies per genotype.

(F) Representative picture of the Smurf assay on 15- to 20-day-old female (top) or male (bottom) flies. Scale bar, 500 μm.

(G) Survival of $esg^{GFP}>w^{1118}$, $esg^{GFP}>$*Pex5*-i, $esg^{GFP}>$*ERp60*-i, and $esg^{GFP}>$*Pex5*-i;*ERp60*-i male flies.

(H) Survival of $esg^{GFP}>w^{1118}$, $esg^{GFP}>$*Pex5*-i, $esg^{GFP}>$*ERp60*-i, and $esg^{GFP}>$*Pex5*-i;*ERp60*-i female flies. *n* = 100 flies per genotype. Significance was determined using the Kaplan Meier and log-rank test in (A, B, G, and H). A one-way ANOVA test was used in (C and E). $^{****}p < 0.0001$; $^{***}p < 0.001$; $^{*}p < 0.05$; ns, not significant. See also Figure S7.

regulating PG homeostasis and intestinal health. We identified the ER as a sensor of lipid dysfunction in PG, which activates the UPR to promote ISC proliferation and control epithelial regeneration.

Ether phospholipids are essential components of the plasma and organelle membranes, and alteration in their metabolism can affect signaling pathways.[33,76] Moreover, ether lipids are also antioxidants and contribute to maintaining a healthy oxidative status in cells. A drop in ether lipids affects other essential membrane lipids, such as phosphatidylcholine (PC) and phosphatidyl ethanolamine (PE). This impacts the PC:PE ratio and affects membrane function and cellular signaling, leading to cell death,[77,104] and is linked to many pathological conditions.[77,82,83] In agreement with previous reports,[76] we found that ether PC and ether PE as well as regular PC and PE and PC:PE ratios changed in $esg^{GFP}>$*Pex5*-i midguts compared to what was observed in control midguts.

Ether lipids synthesis occurs between peroxisome and ER. We found that the depletion of a key enzyme of peroxisomal ether phospholipid metabolism, GNPAT, in PG yields a phenocopy of the increase in PG number observed in $esg^{GFP}>$*Pex5*-i midguts. Activation of the GNPAT catalyzes the conversion of dihydroxyacetone phosphate (DHAP)[105] and acyl-CoA into CoA and acyl-DHAP, which is then transferred to the ER to produce the ether phospholipids.[27] Dietary treatment of 3-day-old $esg^{GFP}>w^{1118}$ and $esg^{GFP}>$*Pex5*-i flies with an acyl-DHAP, 1-*O*-Octadecyl-rac-glycerol (batyl alcohol) restored the number of PG in $esg^{GFP}>$*Pex5*-i flies to numbers observed in control midguts, suggesting that ether phospholipids are the primary regulator of the increase in PG number in $esg^{GFP}>$*Pex5*-i flies.

The ER can sense lipid imbalances in the cell or cell membranes, a state of lipid toxicity that affects proteins and may cause an accumulation of unfolded protein[35,80] that, in turn, activates the UPR response.[35,78,80,106] Under stress, the ER activates three distinct signaling pathways to restore homeostasis.[41,86] The signaling pathways of UPR are mediated by three ER-resident proteins: IRE1 (inositol-requiring enzyme 1), PERK (protein kinase R-like ER kinase), and ATF6 (activating transcription factor 6). IRE1 has serine/threonine kinase and RNase domains in the cytoplasmic region. Upon ER stress, PERK activation triggers the phosphorylation of the serine 51 residue of

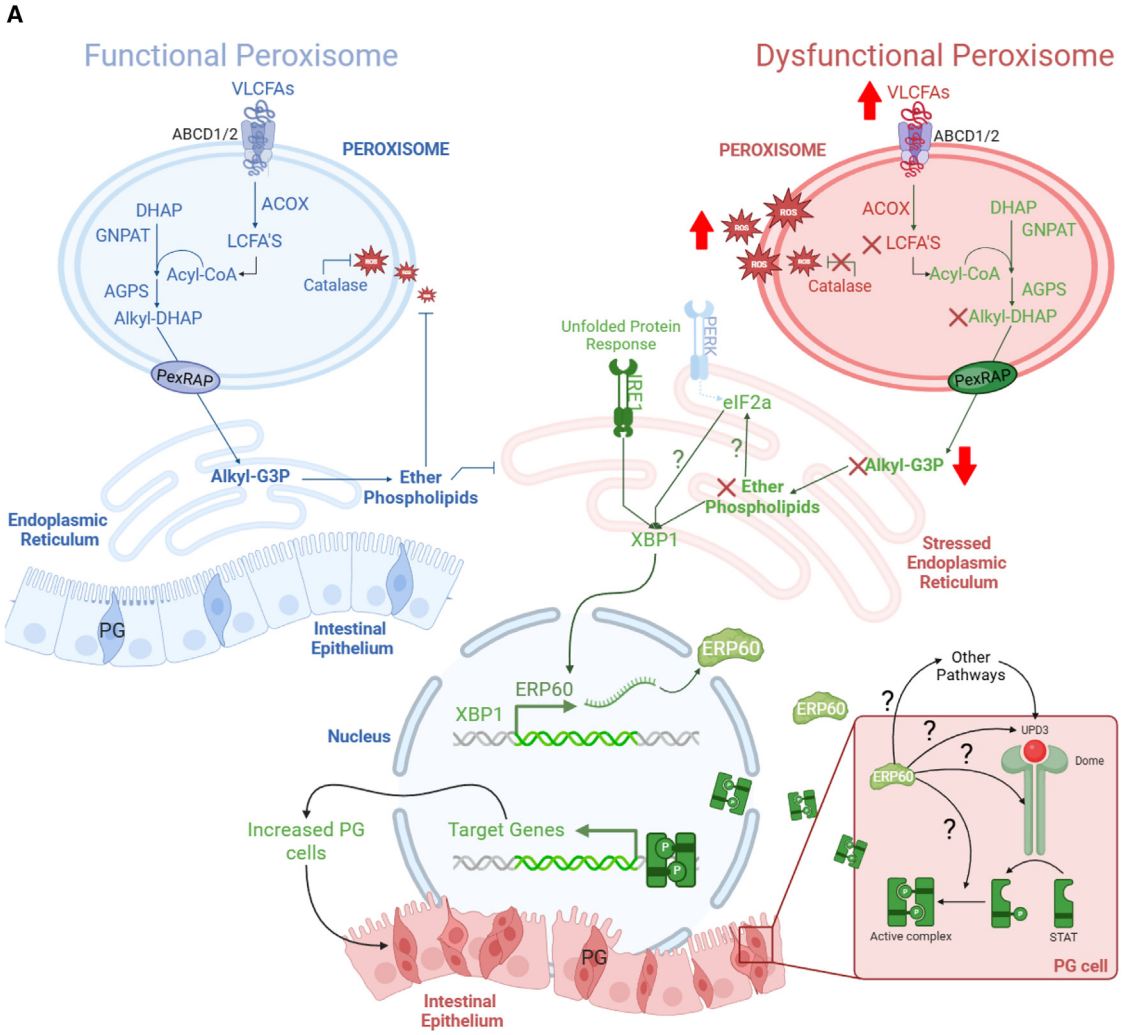

Figure 7. Graphical representation of the results

(A) Alteration of peroxisome biogenesis in PG leads to metabolic dysfunction (right side). Defective peroxisomes cannot process VLCFAs and redox activities and inhibit ether phospholipids synthesis as they fail to produce the Alkyl-G3P precursors used by the ER to make ether phospholipids. Deficiency in ether phospholipids production triggers EIF2α and Xbp1 activation, which leads to the upregulation of ERp60. High levels of ERp60 directly or indirectly support Jak/Stat-mediated proliferation of progenitor cells. Question marks on connecting arrows indicate pathways that have not been molecularly defined. The faint blue arrowhead between Perk and EIF2α denotes a lack of activation of this branch of the pathway in our system.

eIF2α, resulting in the alleviation of ER stress by attenuating translation. IRE1 is activated and recognizes the stem-loop structure of Xbp1 mRNA and induces unconventional splicing. The spliced Xbp1 mRNA encodes an active transcription factor that upregulates the expression of UPR target genes, including ER chaperones, ERAD components, and lipid biosynthetic enzymes.[84] ER stress also induces the translocation of ATF6 from the ER to the Golgi apparatus, where ATF6 is cleaved. This proteolytic cleavage produces the N-terminal region of ATF6, which functions as an active transcription factor and upregulates target genes encoding ER chaperones, ERAD components, and XBP1. When ER stress is not resolved, it might induce autophagy and cellular death.

We demonstrated that a drop in ether phospholipids caused by a dysfunction peroxisomal metabolism triggers Xbp1 splicing and the induction of the ERAD and chaperone gene expression. Particularly, we identify ERp60, the *Drosophila* ortholog of protein disulfate isomerase A3 (PDIA3), and target of Xbp1, as an essential regulator of PG number. We found that ERp60 supports the Upd3/Dome/STAT-dependent accumulation of PG, indicating that ERp60 is a newly identified regulator of Jak/STAT-mediated regulation of ISC homeostasis. Moreover, depletion of ERp60 in developing flies or adult life leads to loss of PG and shortening of the intestinal tract. Interestingly, PDIA3 was found to be upregulated in hepatocellular carcinoma[48] in mammals.

ERp60 is a stress response protein that aids the correct folding of proteins. It is mainly located in the ER, which helps the UPR response to relieve ER stress. However, it has also been found in the nucleus and at the plasma membrane, supporting the

idea that its disulfate isomerase activity regulates many proteins during various cellular signaling, including STA3 activity, DNA repair, antigen presentation, cytokine secretion, and promotion of autophagy.[45,47,48]

Here, we propose a model where the ether lipid metabolism-ER stress-ERp60 axis is a core modulator of ISC homeostasis.

It was reported that peroxisomal dysfunction activates only the PERK-eIF2a of UPR in mammals[42,43,62,76,107] and *Drosophila*.[108] Our work demonstrated that peroxisomal lipid dysfunction in ISC and EB triggers the activation of the Xbp1 branch of the stress response and triggers PG proliferation. This increase in proliferation improves survival in adult females but causes damage to the intestinal epithelium and reduces survival in males. These sex-specific outcomes underline the metabolic difference observed in male and female intestines in *Drosophila*[109–112] as in mammals.[105,113] Interestingly, when we previously analyzed the survival of combined male and female esg^{GFP}>*Pex5*-i versus esg^{GFP}>w^{1118}, we observed no difference in survival rate in normal conditions and under infection.[29] This highlights the importance of analyzing males and females in separate assays, as the profound and often opposite differences in sex-specific responses might affect and confound the studies.

Although we found the Xbp1 branch, and not the PERK branch, of the UPR is the main regulator of ER response to metabolic stress in PG, we detected an increase in phosphorylation of eIF2α in esg^{GFP}>*Pex5*-i PG and a consequence reduction in the transcription of ribosomal genes, which indicates a reduction of protein synthesis, another event controlled by the UPR, previously noticed in peroxisome mutant cells.[108] The eIF2α phosphorylation represents a convergence point of different stress pathways known as the "integrated stress response," which is governed by specific kinases activated by inflammation, viral infections, nutrient deprivation, and heme deficiency.[88] Thus, it is possible that the activation of eIF2α is independent of PERK, but the eIF2α-induced inhibition of global translation still contributes to maintaining the intestinal stem cell state.[114–116]

Previously, another group identified the importance of the PERK-eIF2a and Xbp1 branches of the UPR as regulators of intestinal epithelial regeneration and function in adult flies.[37] They reported that PERK integrates both cell-autonomous and non-autonomous ER stress stimuli to induce ISC proliferation and acute regenerative responses. Yet, the chronic engagement of this response becomes deleterious in aging flies.[37] In another line of research, ER stress is linked to increased inflammatory conditions and dysbiosis of the commensal bacteria, leading to high mortality over aging.[38,117–119] Increasing UPR by activating Xbp1-ERAD signaling in ISCs limited ER-stress-associated signaling in ISCs and may benefit tissue homeostasis.

Here, we added to the role of UPR in intestinal regeneration and found that Xbp1-ERp60 signaling in PG is activated in young and old flies upon metabolic stress and triggers a cell-autonomous increase in PG. This response affects the survival of males under metabolic stress. Although *ERp60* over-expression and *Pex5* depletion have similar effects on PG cell numbers in female and male midguts, we observed sex-specific differences in barrier function and lifespan. It has been reported that the regenerative capacity of aging guts in females is stronger than in males,[120] and adult male flies with depletion of peroxisomes in enterocytes are more susceptible to epithelial barrier damage than females.[121]

In conclusion, our study increases the understanding of how cellular stress responses of PG coordinate and maintain intestinal epithelial regeneration in response to metabolic alteration. We identified ERp60 as an unexplored PG survival and proliferation regulator.

Overall, our study provides insight into peroxisomal signaling, ether lipids metabolism, ISC homeostasis, and ER stress signaling in the gut and sheds light on the etiology of pathologies ranging from inflammatory bowel diseases to colorectal cancers caused by alteration of epithelial regeneration.

Limitations of the study

In this study, we identified the importance of ether phospholipid metabolism in intestinal progenitors in maintaining intestinal homeostasis. Additionally, we determined that ERp60, a disulfide isomerase conserved in mammals,[45] responds to defects in the ether phospholipids to promote epithelial regeneration, adding a player in regulating intestinal epithelial homeostasis. There are limitations in our study. Although we genetically demonstrated that ERp60 impacts the Jak/STAT signaling to drive progenitors' proliferation, we have not proved if ERp60 acts as disulfide isomerase directly interacting with Jak or STAT to promote their activity and trigger proliferation. It was reported that PDIA3 in human hepatocellular carcinoma regulates STAT3 by direct interaction.[48] Thus, future studies must define the molecular mechanisms by which ERp60 controls Jak/STAT-mediated proliferation of progenitors in the intestines.

We reported that treatment with batyl alcohol, a peroxisome-derived intermediate necessary to the ER to complete the ether phospholipids synthesis, rescues the defects in intestinal epithelial homeostasis; we did not determine which specific ether phospholipid controls the ER stress response and whether its deficiency is the direct or indirect cause of UPR response. More analyses would define the distinct lipid requirement that controls intestinal epithelial regeneration.

RESOURCE AVAILABILITY

Lead contact

Further information and requests for resources and reagents should be directed to and will be fulfilled by the lead contact, Francesca Di Cara (dicara@dal.ca).

Materials availability

- Plasmid pTWERp60 generated in this study is available to the lead contact upon request.
- *Drosophila* line overexpressing ERp60 (UAS-$Erp60^{OE}$) was generated in this study and is available upon request to the lead contact.

Data and code availability

- RNA sequencing data have been deposited at NCBI and are publicly available as of publication. Accession numbers are listed in the key resources table. The lead contact will share the microscopy data reported in this paper upon request.
- The article does not report any original code.
- The lead contact can provide any additional information required to re-analyze the data reported in this paper upon request.

ACKNOWLEDGMENTS

This work was funded by a Project Grant from the 2019-20 Establishment Grant (Research Nova Scotia), the CIHR Project grant PJT-169179, and NSERC Discovery Grant RGPIN-2019-04083 to Francesca Di Cara. Flow cytometry was performed at the Dalhousie University, Faculty of Medicine Flow Cytometry Core Facility, and microscopy was performed at the Dalhousie University, Faculty of Medicine Cellular and Molecular Digital Imaging. We thank Gerard Gaspard for their help with microscopy and Derek Rowter and Renee Raudonis for training and technical assistance in flow cytometry. The sequencing of the RNA libraries was performed at Génome Québec, Montreal, QC. Metabolomics analysis was performed at the Metabolomics Core Facility at the University of Utah. Mass spectrometry equipment was obtained through NCRR Shared Instrumentation Grant 1S10OD016232-01, 1S10OD018210-01A1, and 1S10OD021505-01. The authors thank Dan Cuthbertson of Agilent Technologies for assistance in implementing iterative exclusion in the tandem mass spectrometry experiments.

AUTHOR CONTRIBUTIONS

S.M. and R.L. executed the experiments and optimized protocols. S.G. isolated intestinal stem cells, extracted total RNA, and made libraries for RNA sequencing; T.W. and M.S. validated the screen hits. A.M. and Y.M. helped with the crosses and gut immunofluorescence. B.D.P. helped with imaging processing and edited the manuscript. F.D. conceived and supervised the project and wrote the manuscript.

DECLARATION OF INTERESTS

The authors declare no competing interests.

STAR★METHODS

Detailed methods are provided in the online version of this paper and include the following:

- KEY RESOURCES TABLE
- EXPERIMENTAL MODEL AND STUDY PARTICIPANT DETAILS
  - Drosophila melanogaster
  - Ethics approval and consent to participate
  - *Pex5* mutant mice
- METHOD DETAILS
  - Cornmeal diet (CMD)
  - High-fat diet (HFD)treatment
  - 1-*O*-Octadecyl-*rac*-glycerol treatment
  - Niacin treatment
  - Tofacitinib treatment
  - Measurement of H_2O_2
  - Free fatty acids (FFA) quantification
  - Progenitors (ISC and EB) isolation, RNA extraction and library preparation for RNA sequencing transcriptomic
  - RNA sequencing analyses
  - RNA-seq enrichment pathway
  - Total RNA extraction, cDNA synthesis and QRT-PCR
  - RT-PCR to test XBp1 splicing
  - Immunofluorescence and confocal microscopy
  - Detection of apoptosis assay
  - Smurf assay
  - Lipidomics
  - Mouse intestinal organoids culture
- QUANTIFICATION AND STATISTICAL ANALYSIS
  - Statistical analyses
  - Quantification of agarose gel band signals
  - Quantification of GFP+ cells in midguts
  - Quantification of fluorescence signals

SUPPLEMENTAL INFORMATION

Supplemental information can be found online at https://doi.org/10.1016/j.isci.2025.111946.

Received: August 14, 2024
Revised: December 7, 2024
Accepted: January 30, 2025
Published: February 4, 2025

REFERENCES

1. Vereecke, L., Beyaert, R., and van Loo, G. (2011). Enterocyte death and intestinal barrier maintenance in homeostasis and disease. Trends Mol. Med. *17*, 584–593. https://doi.org/10.1016/j.molmed.2011.05.011.
2. Lemaitre, B., and Miguel-Aliaga, I. (2013). The digestive tract of Drosophila melanogaster. Annu. Rev. Genet. *47*, 377–404. https://doi.org/10.1146/annurev-genet-111212-133343.
3. Capo, F., Wilson, A., and Di Cara, F. (2019). The Intestine of Drosophila melanogaster: An Emerging Versatile Model System to Study Intestinal Epithelial Homeostasis and Host-Microbial Interactions in Humans. Microorganisms *7*, 336. https://doi.org/10.3390/microorganisms7090336.
4. Jiang, H., and Edgar, B.A. (2009). EGFR signaling regulates the proliferation of Drosophila adult midgut progenitors. Development *136*, 483–493. https://doi.org/10.1242/dev.026955.
5. Ohlstein, B., and Spradling, A. (2006). The adult Drosophila posterior midgut is maintained by pluripotent stem cells. Nature *439*, 470–474. https://doi.org/10.1038/nature04333.
6. Jiang, H., and Edgar, B.A. (2011). Intestinal stem cells in the adult Drosophila midgut. Exp. Cell Res. *317*, 2780–2788. https://doi.org/10.1016/j.yexcr.2011.07.020.
7. Kolev, H.M., and Kaestner, K.H. (2023). Mammalian Intestinal Development and Differentiation-The State of the Art. Cell. Mol. Gastroenterol. Hepatol. *16*, 809–821. https://doi.org/10.1016/j.jcmgh.2023.07.011.
8. Pesic, M., and Greten, F.R. (2016). Inflammation and cancer: tissue regeneration gone awry. Curr. Opin. Cell Biol. *43*, 55–61. https://doi.org/10.1016/j.ceb.2016.07.010.
9. Apidianakis, Y., Pitsouli, C., Perrimon, N., and Rahme, L. (2009). Synergy between bacterial infection and genetic predisposition in intestinal dysplasia. Proc. Natl. Acad. Sci. USA *106*, 20883–20888. https://doi.org/10.1073/pnas.0911797106.
10. Jiang, H., Patel, P.H., Kohlmaier, A., Grenley, M.O., McEwen, D.G., and Edgar, B.A. (2009). Cytokine/Jak/Stat signaling mediates regeneration and homeostasis in the Drosophila midgut. Cell *137*, 1343–1355. https://doi.org/10.1016/j.cell.2009.05.014.
11. Vanuytsel, T., Senger, S., Fasano, A., and Shea-Donohue, T. (2013). Major signaling pathways in intestinal stem cells. Biochim. Biophys. Acta *1830*, 2410–2426. https://doi.org/10.1016/j.bbagen.2012.08.006.
12. Miguel-Aliaga, I., Jasper, H., and Lemaitre, B. (2018). Anatomy and Physiology of the Digestive Tract of Drosophila melanogaster. Gene *210*, 357–396. https://doi.org/10.1534/genetics.118.300224.
13. Urbauer, E., Rath, E., and Haller, D. (2020). Mitochondrial Metabolism in the Intestinal Stem Cell Niche-Sensing and Signaling in Health and Disease. Front. Cell Dev. Biol. *8*, 602814. https://doi.org/10.3389/fcell.2020.602814.
14. Tiwari, S.K., and Mandal, S. (2021). Mitochondrial Control of Stem Cell State and Fate: Lessons From Drosophila. Front. Cell Dev. Biol. *9*, 606639. https://doi.org/10.3389/fcell.2021.606639.
15. Wang, D., Odle, J., and Liu, Y. (2021). Metabolic Regulation of Intestinal Stem Cell Homeostasis. Trends Cell Biol. *31*, 325–327. https://doi.org/10.1016/j.tcb.2021.02.001.
16. Rodriguez-Colman, M.J., Schewe, M., Meerlo, M., Stigter, E., Gerrits, J., Pras-Raves, M., Sacchetti, A., Hornsveld, M., Oost, K.C., Snippert, H.J., et al. (2017). Interplay between metabolic identities in the intestinal crypt

supports stem cell function. Nature *543*, 424–427. https://doi.org/10.1038/nature21673.

17. Mihaylova, M.M., Cheng, C.W., Cao, A.Q., Tripathi, S., Mana, M.D., Bauer-Rowe, K.E., Abu-Remaileh, M., Clavain, L., Erdemir, A., Lewis, C.A., et al. (2018). Fasting Activates Fatty Acid Oxidation to Enhance Intestinal Stem Cell Function during Homeostasis and Aging. Cell Stem Cell *22*, 769–778.e4. https://doi.org/10.1016/j.stem.2018.04.001.
18. Morris, O., Deng, H., Tam, C., and Jasper, H. (2020). Warburg-like Metabolic Reprogramming in Aging Intestinal Stem Cells Contributes to Tissue Hyperplasia. Cell Rep. *33*, 108423. https://doi.org/10.1016/j.celrep.2020.108423.
19. Berger, E., Rath, E., Yuan, D., Waldschmitt, N., Khaloian, S., Allgäuer, M., Staszewski, O., Lobner, E.M., Schöttl, T., Giesbertz, P., et al. (2016). Mitochondrial function controls intestinal epithelial stemness and proliferation. Nat. Commun. *7*, 13171. https://doi.org/10.1038/ncomms13171.
20. Zhang, F., Pirooznia, M., and Xu, H. (2020). Mitochondria regulate intestinal stem cell proliferation and epithelial homeostasis through FOXO. Mol. Biol. Cell *31*, 1538–1549. https://doi.org/10.1091/mbc.E19-10-0560.
21. Khaloian, S., Rath, E., Hammoudi, N., Gleisinger, E., Blutke, A., Giesbertz, P., Berger, E., Metwaly, A., Waldschmitt, N., Allez, M., and Haller, D. (2020). Mitochondrial impairment drives intestinal stem cell transition into dysfunctional Paneth cells predicting Crohn's disease recurrence. Gut *69*, 1939–1951. https://doi.org/10.1136/gutjnl-2019-319514.
22. Zhang, C., Jin, Y., Marchetti, M., Lewis, M.R., Hammouda, O.T., and Edgar, B.A. (2022). EGFR signaling activates intestinal stem cells by promoting mitochondrial biogenesis and beta-oxidation. Curr. Biol. *32*, 3704–3719.e7. https://doi.org/10.1016/j.cub.2022.07.003.
23. Chen, L., Vasoya, R.P., Toke, N.H., Parthasarathy, A., Luo, S., Chiles, E., Flores, J., Gao, N., Bonder, E.M., Su, X., and Verzi, M.P. (2020). HNF4 Regulates Fatty Acid Oxidation and Is Required for Renewal of Intestinal Stem Cells in Mice. Gastroenterology *158*, 985–999.e9. https://doi.org/10.1053/j.gastro.2019.11.031.
24. Domingues, N., Pires, J., Milosevic, I., and Raimundo, N. (2025). Role of lipids in interorganelle communication. Trends Cell Biol. *35*, 46–58. https://doi.org/10.1016/j.tcb.2024.04.008.
25. Redhai, S., and Boutros, M. (2021). The Role of Organelles in Intestinal Function, Physiology, and Disease. Trends Cell Biol. *31*, 485–499. https://doi.org/10.1016/j.tcb.2021.01.003.
26. Apidianakis, Y., and Rahme, L.G. (2011). Drosophila melanogaster as a model for human intestinal infection and pathology. Dis. Model. Mech. *4*, 21–30. https://doi.org/10.1242/dmm.003970.
27. Wanders, R.J.A., and Waterham, H.R. (2006). Biochemistry of mammalian peroxisomes revisited. Annu. Rev. Biochem. *75*, 295–332. https://doi.org/10.1146/annurev.biochem.74.082803.133329.
28. Waterham, H.R., Ferdinandusse, S., and Wanders, R.J.A. (2016). Human disorders of peroxisome metabolism and biogenesis. Biochim. Biophys. Acta *1863*, 922–933. https://doi.org/10.1016/j.bbamcr.2015.11.015.
29. Di Cara, F., Bülow, M.H., Simmonds, A.J., and Rachubinski, R.A. (2018). Dysfunctional peroxisomes compromise gut structure and host defense by increased cell death and Tor-dependent autophagy. Mol. Biol. Cell *29*, 2766–2783. https://doi.org/10.1091/mbc.E18-07-0434.
30. Du, G., Xiong, L., Li, X., Zhuo, Z., Zhuang, X., Yu, Z., Wu, L., Xiao, D., Liu, Z., Jie, M., et al. (2020). Peroxisome Elevation Induces Stem Cell Differentiation and Intestinal Epithelial Repair. Dev. Cell *53*, 169–184.e11. https://doi.org/10.1016/j.devcel.2020.03.002.
31. Plongthongkum, N., Kullawong, N., Panyim, S., and Tirasophon, W. (2007). Ire1 regulated XBP1 mRNA splicing is essential for the unfolded protein response (UPR) in Drosophila melanogaster. Biochem. Biophys. Res. Commun. *354*, 789–794. https://doi.org/10.1016/j.bbrc.2007.01.056.
32. Sicari, D., Delaunay-Moisan, A., Combettes, L., Chevet, E., and Igbaria, A. (2020). A guide to assessing endoplasmic reticulum homeostasis and stress in mammalian systems. FEBS J. *287*, 27–42. https://doi.org/10.1111/febs.15107.
33. Dean, J.M., and Lodhi, I.J. (2018). Structural and functional roles of ether lipids. Protein Cell *9*, 196–206. https://doi.org/10.1007/s13238-017-0423-5.
34. Han, J., and Kaufman, R.J. (2016). The role of ER stress in lipid metabolism and lipotoxicity. J. Lipid Res. *57*, 1329–1338. https://doi.org/10.1194/jlr.R067595.
35. Halbleib, K., Pesek, K., Covino, R., Hofbauer, H.F., Wunnicke, D., Hänelt, I., Hummer, G., and Ernst, R. (2017). Activation of the Unfolded Protein Response by Lipid Bilayer Stress. Mol. Cell *67*, 673–684.e8. https://doi.org/10.1016/j.molcel.2017.06.012.
36. Madsen, S., Ramosaj, M., and Knobloch, M. (2021). Lipid metabolism in focus: how the build-up and breakdown of lipids affects stem cells. Development *148*, dev191924. https://doi.org/10.1242/dev.191924.
37. Wang, L., Ryoo, H.D., Qi, Y., and Jasper, H. (2015). PERK Limits Drosophila Lifespan by Promoting Intestinal Stem Cell Proliferation in Response to ER Stress. PLoS Genet. *11*, e1005220. https://doi.org/10.1371/journal.pgen.1005220.
38. Wang, L., Zeng, X., Ryoo, H.D., and Jasper, H. (2014). Integration of UPRER and oxidative stress signaling in the control of intestinal stem cell proliferation. PLoS Genet. *10*, e1004568. https://doi.org/10.1371/journal.pgen.1004568.
39. Hetz, C., and Papa, F.R. (2018). The Unfolded Protein Response and Cell Fate Control. Mol. Cell *69*, 169–181. https://doi.org/10.1016/j.molcel.2017.06.017.
40. Harding, H.P., Calfon, M., Urano, F., Novoa, I., and Ron, D. (2002). Transcriptional and translational control in the Mammalian unfolded protein response. Annu. Rev. Cell. Dev. Biol. *18*, 575–599. https://doi.org/10.1146/annurev.cellbio.18.011402.160624.
41. Walter, P., and Ron, D. (2011). The unfolded protein response: from stress pathway to homeostatic regulation. Science *334*, 1081–1086. https://doi.org/10.1126/science.1209038.
42. He, A., Dean, J.M., and Lodhi, I.J. (2021). Peroxisomes as cellular adaptors to metabolic and environmental stress. Trends Cell Biol. *31*, 656–670. https://doi.org/10.1016/j.tcb.2021.02.005.
43. Kovacs, W.J., Charles, K.N., Walter, K.M., Shackelford, J.E., Wikander, T.M., Richards, M.J., Fliesler, S.J., Krisans, S.K., and Faust, P.L. (2012). Peroxisome deficiency-induced ER stress and SREBP-2 pathway activation in the liver of newborn PEX2 knock-out mice. Biochim. Biophys. Acta *1821*, 895–907. https://doi.org/10.1016/j.bbalip.2012.02.011.
44. Park, S.M., Kang, T.I., and So, J.S. (2021). Roles of XBP1s in Transcriptional Regulation of Target Genes. Biomedicine *9*, 791. https://doi.org/10.3390/biomedicines9070791.
45. Chichiarelli, S., Altieri, F., Paglia, G., Rubini, E., Minacori, M., and Eufemi, M. (2022). ERp57/PDIA3: new insight. Cell. Mol. Biol. Lett. *27*, 12. https://doi.org/10.1186/s11658-022-00315-x.
46. Santana-Codina, N., Carretero, R., Sanz-Pamplona, R., Cabrera, T., Guney, E., Oliva, B., Clezardin, P., Olarte, O.E., Loza-Alvarez, P., Méndez-Lucas, A., et al. (2013). A transcriptome-proteome integrated network identifies endoplasmic reticulum thiol oxidoreductase (ERp57) as a hub that mediates bone metastasis. Mol. Cell. Proteomics *12*, 2111–2125. https://doi.org/10.1074/mcp.M112.022772.
47. Aureli, C., Gaucci, E., Arcangeli, V., Grillo, C., Eufemi, M., and Chichiarelli, S. (2013). ERp57/PDIA3 binds specific DNA fragments in a melanoma cell line. Gene *524*, 390–395. https://doi.org/10.1016/j.gene.2013.04.004.
48. Kondo, R., Ishino, K., Wada, R., Takata, H., Peng, W.X., Kudo, M., Kure, S., Kaneya, Y., Taniai, N., Yoshida, H., and Naito, Z. (2019). Downregulation of protein disulfide-isomerase A3 expression inhibits cell proliferation and induces apoptosis through STAT3 signaling in hepatocellular carcinoma. Int. J. Oncol. *54*, 1409–1421. https://doi.org/10.3892/ijo.2019.4710.

49. Ghemrawi, R., Battaglia-Hsu, S.F., and Arnold, C. (2018). Endoplasmic Reticulum Stress in Metabolic Disorders. Cell *7*, 63. https://doi.org/10.3390/cells7060063.

50. Smith, J.J., and Aitchison, J.D. (2013). Peroxisomes take shape. Nat. Rev. Mol. Cell Biol. *14*, 803–817. https://doi.org/10.1038/nrm3700.

51. Walker, C.L., Pomatto, L.C.D., Tripathi, D.N., and Davies, K.J.A. (2018). Redox Regulation of Homeostasis and Proteostasis in Peroxisomes. Physiol. Rev. *98*, 89–115. https://doi.org/10.1152/physrev.00033.2016.

52. Nath, A.S., Parsons, B.D., Makdissi, S., Chilvers, R.L., Mu, Y., Weaver, C.M., Euodia, I., Fitze, K.A., Long, J., Scur, M., et al. (2022). Modulation of the cell membrane lipid milieu by peroxisomal beta-oxidation induces Rho1 signaling to trigger inflammatory responses. Cell Rep. *38*, 110433. https://doi.org/10.1016/j.celrep.2022.110433.

53. Dutta, D., Dobson, A.J., Houtz, P.L., Gläßer, C., Revah, J., Korzelius, J., Patel, P.H., Edgar, B.A., and Buchon, N. (2015). Regional Cell-Specific Transcriptome Mapping Reveals Regulatory Complexity in the Adult Drosophila Midgut. Cell Rep. *12*, 346–358. https://doi.org/10.1016/j.celrep.2015.06.009.

54. Reimand, J., Isserlin, R., Voisin, V., Kucera, M., Tannus-Lopes, C., Rostamianfar, A., Wadi, L., Meyer, M., Wong, J., Xu, C., et al. (2019). Pathway enrichment analysis and visualization of omics data using g:Profiler, GSEA, Cytoscape and EnrichmentMap. Nat. Protoc. *14*, 482–517. https://doi.org/10.1038/s41596-018-0103-9.

55. Wangler, M.F., Chao, Y.H., Bayat, V., Giagtzoglou, N., Shinde, A.B., Putluri, N., Coarfa, C., Donti, T., Graham, B.H., Faust, J.E., et al. (2017). Peroxisomal biogenesis is genetically and biochemically linked to carbohydrate metabolism in Drosophila and mouse. PLoS Genet. *13*, e1006825. https://doi.org/10.1371/journal.pgen.1006825.

56. Herzog, K., Pras-Raves, M.L., Vervaart, M.A.T., Luyf, A.C.M., van Kampen, A.H.C., Wanders, R.J.A., Waterham, H.R., and Vaz, F.M. (2016). Lipidomic analysis of fibroblasts from Zellweger spectrum disorder patients identifies disease-specific phospholipid ratios. J. Lipid Res. *57*, 1447–1454. https://doi.org/10.1194/jlr.M067470.

57. Di Cara, F., Sheshachalam, A., Braverman, N.E., Rachubinski, R.A., and Simmonds, A.J. (2017). Peroxisome-Mediated Metabolism Is Required for Immune Response to Microbial Infection. Immunity *47*, 93–106.e7. https://doi.org/10.1016/j.immuni.2017.06.016.

58. Shaw, R.L., Kohlmaier, A., Polesello, C., Veelken, C., Edgar, B.A., and Tapon, N. (2010). The Hippo pathway regulates intestinal stem cell proliferation during Drosophila adult midgut regeneration. Development *137*, 4147–4158. https://doi.org/10.1242/dev.052506.

59. Xu, N., Wang, S.Q., Tan, D., Gao, Y., Lin, G., and Xi, R. (2011). EGFR, Wingless and JAK/STAT signaling cooperatively maintain Drosophila intestinal stem cells. Dev. Biol. *354*, 31–43. https://doi.org/10.1016/j.ydbio.2011.03.018.

60. Vembar, S.S., and Brodsky, J.L. (2008). One step at a time: endoplasmic reticulum-associated degradation. Nat. Rev. Mol. Cell Biol. *9*, 944–957. https://doi.org/10.1038/nrm2546.

61. Hetz, C., Zhang, K., and Kaufman, R.J. (2020). Mechanisms, regulation and functions of the unfolded protein response. Nat. Rev. Mol. Cell Biol. *21*, 421–438. https://doi.org/10.1038/s41580-020-0250-z.

62. Kovacs, W.J., Tape, K.N., Shackelford, J.E., Wikander, T.M., Richards, M.J., Fliesler, S.J., Krisans, S.K., and Faust, P.L. (2009). Peroxisome deficiency causes a complex phenotype because of hepatic SREBP/Insig dysregulation associated with endoplasmic reticulum stress. J. Biol. Chem. *284*, 7232–7245. https://doi.org/10.1074/jbc.M809064200.

63. Du, G., Liu, Z., Yu, Z., Zhuo, Z., Zhu, Y., Zhou, J., Li, Y., and Chen, H. (2021). Taurine represses age-associated gut hyperplasia in Drosophila via counteracting endoplasmic reticulum stress. Aging Cell *20*, e13319. https://doi.org/10.1111/acel.13319.

64. Koivunen, P., Helaakoski, T., Annunen, P., Veijola, J., Räisänen, S., Pihlajaniemi, T., and Kivirikko, K.I. (1996). ERp60 does not substitute for protein disulphide isomerase as the beta-subunit of prolyl 4-hydroxylase. Biochem. J. *316*, 599–605. https://doi.org/10.1042/bj3160599.

65. Phillips, M.D., and Thomas, C.M. (2006). Brush border spectrin is required for early endosome recycling in Drosophila. J. Cell Sci. *119*, 1361–1370. https://doi.org/10.1242/jcs.02839.

66. Meghnem, D., Leong, E., Pinelli, M., Marshall, J.S., and Di Cara, F. (2022). Peroxisomes Regulate Cellular Free Fatty Acids to Modulate Mast Cell TLR2, TLR4, and IgE-Mediated Activation. Front. Cell Dev. Biol. *10*, 856243. https://doi.org/10.3389/fcell.2022.856243.

67. Bulow, M.H., Wingen, C., Senyilmaz, D., Gosejacob, D., Sociale, M., Bauer, R., Schulze, H., Sandhoff, K., Teleman, A.A., Hoch, M., and Sellin, J. (2018). Unbalanced lipolysis results in lipotoxicity and mitochondrial damage in peroxisome-deficient Pex19 mutants. Mol. Biol. Cell *29*, 396–407. https://doi.org/10.1091/mbc.E17-08-0535.

68. Nayak, N., and Mishra, M. (2021). High fat diet induced abnormalities in metabolism, growth, behavior, and circadian clock in Drosophila melanogaster. Life Sci. *281*, 119758. https://doi.org/10.1016/j.lfs.2021.119758.

69. Zhao, X., and Karpac, J. (2020). The Drosophila midgut and the systemic coordination of lipid-dependent energy homeostasis. Curr. Opin. Insect Sci. *41*, 100–105. https://doi.org/10.1016/j.cois.2020.07.003.

70. Nelson, R.H., Vlazny, D., Smailovic, A., and Miles, J.M. (2012). Intravenous niacin acutely improves the efficiency of dietary fat storage in lean and obese humans. Diabetes *61*, 3172–3175. https://doi.org/10.2337/db12-0236.

71. Gouni-Berthold, I., and Berthold, H.K. (2013). The role of niacin in lipid-lowering treatment: are we aiming too high? Curr. Pharm. Des. *19*, 3094–3106. https://doi.org/10.2174/1381612811319170017.

72. Jia, H., Li, X., Gao, H., Feng, Z., Li, X., Zhao, L., Jia, X., Zhang, H., and Liu, J. (2008). High doses of nicotinamide prevent oxidative mitochondrial dysfunction in a cellular model and improve motor deficit in a Drosophila model of Parkinson's disease. J. Neurosci. Res. *86*, 2083–2090. https://doi.org/10.1002/jnr.21650.

73. Samad, N., Manzoor, N., Batool, A., Noor, A., Khaliq, S., Aurangzeb, S., Bhatti, S.A., and Imran, I. (2023). Protective effects of niacin following high fat rich diet: an in-vivo and in-silico study. Sci. Rep. *13*, 21343. https://doi.org/10.1038/s41598-023-48566-8.

74. Chornyi, S., Ofman, R., Koster, J., and Waterham, H.R. (2023). The origin of long-chain fatty acids required for de novo ether lipid/plasmalogen synthesis. J. Lipid Res. *64*, 100364. https://doi.org/10.1016/j.jlr.2023.100364.

75. Nagan, N., and Zoeller, R.A. (2001). Plasmalogens: biosynthesis and functions. Prog. Lipid Res. *40*, 199–229. https://doi.org/10.1016/s0163-7827(01)00003-0.

76. Lodhi, I.J., Wei, X., Yin, L., Feng, C., Adak, S., Abou-Ezzi, G., Hsu, F.F., Link, D.C., and Semenkovich, C.F. (2015). Peroxisomal lipid synthesis regulates inflammation by sustaining neutrophil membrane phospholipid composition and viability. Cell Metab. *21*, 51–64. https://doi.org/10.1016/j.cmet.2014.12.002.

77. Li, Z., Agellon, L.B., Allen, T.M., Umeda, M., Jewell, L., Mason, A., and Vance, D.E. (2006). The ratio of phosphatidylcholine to phosphatidylethanolamine influences membrane integrity and steatohepatitis. Cell Metab. *3*, 321–331. https://doi.org/10.1016/j.cmet.2006.03.007.

78. Volmer, R., and Ron, D. (2015). Lipid-dependent regulation of the unfolded protein response. Curr. Opin. Cell Biol. *33*, 67–73. https://doi.org/10.1016/j.ceb.2014.12.002.

79. Hou, N.S., and Taubert, S. (2014). Membrane lipids and the endoplasmic reticulum unfolded protein response: An interesting relationship. Worm *3*, e962405. https://doi.org/10.4161/21624046.2014.962405.

80. Koh, J.H., Wang, L., Beaudoin-Chabot, C., and Thibault, G. (2018). Lipid bilayer stress-activated IRE-1 modulates autophagy during endoplasmic reticulum stress. J. Cell Sci. *131*, jcs217992. https://doi.org/10.1242/jcs.217992.

81. Jacquemyn, J., Cascalho, A., and Goodchild, R.E. (2017). The ins and outs of endoplasmic reticulum-controlled lipid biosynthesis. EMBO Rep. *18*, 1905–1921. https://doi.org/10.15252/embr.201643426.

82. Kim, Y.J., Lee, H.S., Kim, Y.K., Park, S., Kim, J.M., Yun, J.H., Yu, H.Y., and Kim, B.J. (2016). Association of Metabolites with Obesity and Type 2 Diabetes Based on FTO Genotype. PLoS One *11*, e0156612. https://doi.org/10.1371/journal.pone.0156612.

83. Mitsuhashi, S., and Nishino, I. (2011). Phospholipid synthetic defect and mitophagy in muscle disease. Autophagy *7*, 1559–1561. https://doi.org/10.4161/auto.7.12.17925.

84. Lee, A.H., Iwakoshi, N.N., and Glimcher, L.H. (2003). XBP-1 regulates a subset of endoplasmic reticulum resident chaperone genes in the unfolded protein response. Mol. Cell Biol. *23*, 7448–7459. https://doi.org/10.1128/MCB.23.21.7448-7459.2003.

85. Chen, X., Shi, C., He, M., Xiong, S., and Xia, X. (2023). Endoplasmic reticulum stress: molecular mechanism and therapeutic targets. Signal Transduct. Targeted Ther. *8*, 352. https://doi.org/10.1038/s41392-023-01570-w.

86. Ryoo, H.D., and Steller, H. (2007). Unfolded protein response in Drosophila: why another model can make it fly. Cell Cycle *6*, 830–835. https://doi.org/10.4161/cc.6.7.4064.

87. Travers, K.J., Patil, C.K., Wodicka, L., Lockhart, D.J., Weissman, J.S., and Walter, P. (2000). Functional and genomic analyses reveal an essential coordination between the unfolded protein response and ER-associated degradation. Cellule *101*, 249–258. https://doi.org/10.1016/s0092-8674(00)80835-1.

88. Pakos-Zebrucka, K., Koryga, I., Mnich, K., Ljujic, M., Samali, A., and Gorman, A.M. (2016). The integrated stress response. EMBO Rep. *17*, 1374–1395. https://doi.org/10.15252/embr.201642195.

89. Ryoo, H.D., Domingos, P.M., Kang, M.J., and Steller, H. (2007). Unfolded protein response in a Drosophila model for retinal degeneration. EMBO. J. *26*, 242–252. https://doi.org/10.1038/sj.emboj.7601477.

90. Lakshmanan, A.P., Harima, M., Suzuki, K., Soetikno, V., Nagata, M., Nakamura, T., Takahashi, T., Sone, H., Kawachi, H., and Watanabe, K. (2013). The hyperglycemia stimulated myocardial endoplasmic reticulum (ER) stress contributes to diabetic cardiomyopathy in the transgenic non-obese type 2 diabetic rats: a differential role of unfolded protein response (UPR) signaling proteins. Int. J. Biochem. Cell Biol. *45*, 438–447. https://doi.org/10.1016/j.biocel.2012.09.017.

91. Eckl, E.M., Ziegemann, O., Krumwiede, L., Fessler, E., and Jae, L.T. (2021). Sensing, signaling and surviving mitochondrial stress. Cell. Mol. Life Sci. *78*, 5925–5951. https://doi.org/10.1007/s00018-021-03887-7.

92. Morrow, G., Le Pécheur, M., and Tanguay, R.M. (2016). Drosophila melanogaster mitochondrial Hsp22: a role in resistance to oxidative stress, aging and the mitochondrial unfolding protein response. Biogerontology *17*, 61–70. https://doi.org/10.1007/s10522-015-9591-y.

93. Wood, J.G., Schwer, B., Wickremesinghe, P.C., Hartnett, D.A., Burhenn, L., Garcia, M., Li, M., Verdin, E., and Helfand, S.L. (2018). Sirt4 is a mitochondrial regulator of metabolism and lifespan in Drosophila melanogaster. Proc. Natl. Acad. Sci. USA *115*, 1564–1569. https://doi.org/10.1073/pnas.1720673115.

94. Tang, B.L. (2016). Sirt1 and the Mitochondria. Mol. Cell. *39*, 87–95. https://doi.org/10.14348/molcells.2016.2318.

95. Barry, W.E., and Thummel, C.S. (2016). The Drosophila HNF4 nuclear receptor promotes glucose-stimulated insulin secretion and mitochondrial function in adults. Elife *5*, e11183. https://doi.org/10.7554/eLife.11183.

96. Lees, J., Pèrtille, F., Løtvedt, P., Jensen, P., and Bosagna, C.G. (2023). The mitoepigenome responds to stress, suggesting novel mito-nuclear interactions in vertebrates. BMC Genom. *24*, 561. https://doi.org/10.1186/s12864-023-09668-9.

97. Doupe, D.P., Marshall, O.J., Dayton, H., Brand, A.H., and Perrimon, N. (2018). Drosophila intestinal stem and progenitor cells are major sources and regulators of homeostatic niche signals. Proc. Natl. Acad. Sci. USA *115*, 12218–12223. https://doi.org/10.1073/pnas.1719169115.

98. Guo, Z., Lucchetta, E., Rafel, N., and Ohlstein, B. (2016). Maintenance of the adult Drosophila intestine: all roads lead to homeostasis. Curr. Opin. Genet. Dev. *40*, 81–86. https://doi.org/10.1016/j.gde.2016.06.009.

99. Herrera, S.C., and Bach, E.A. (2019). JAK/STAT signaling in stem cells and regeneration: from Drosophila to vertebrates. Development *146*, dev167643. https://doi.org/10.1242/dev.167643.

100. Bangi, E., Smibert, P., Uzilov, A.V., Teague, A.G., Gopinath, S., Antipin, Y., Chen, R., Hecht, C., Gruszczynski, N., Yon, W.J., et al. (2021). A Drosophila platform identifies a novel, personalized therapy for a patient with adenoid cystic carcinoma. iScience *24*, 102212. https://doi.org/10.1016/j.isci.2021.102212.

101. Vyas, D., O'Dell, K.M., Bandy, J.L., and Boyce, E.G. (2013). Tofacitinib: The First Janus Kinase (JAK) inhibitor for the treatment of rheumatoid arthritis. Ann. Pharmacother. *47*, 1524–1531. https://doi.org/10.1177/1060028013512790.

102. Wong, R., Piper, M.D.W., Wertheim, B., and Partridge, L. (2009). Quantification of Food Intake in Drosophila. PLoS One *4*, 6063. https://doi.org/10.1371/JOURNAL.PONE.0006063.

103. Rera, M., Bahadorani, S., Cho, J., Koehler, C.L., Ulgherait, M., Hur, J.H., Ansari, W.S., Lo, T., Jr., Jones, D.L., and Walker, D.W. (2011). Modulation of longevity and tissue homeostasis by the Drosophila PGC-1 homolog. Cell Metab. *14*, 623–634. https://doi.org/10.1016/j.cmet.2011.09.013.

104. van der Veen, J.N., Kennelly, J.P., Wan, S., Vance, J.E., Vance, D.E., and Jacobs, R.L. (2017). The critical role of phosphatidylcholine and phosphatidylethanolamine metabolism in health and disease. Biochim. Biophys. Acta Biomembr. *1859*, 1558–1572. https://doi.org/10.1016/j.bbamem.2017.04.006.

105. Baars, A., Oosting, A., Lohuis, M., Koehorst, M., El Aidy, S., Hugenholtz, F., Smidt, H., Mischke, M., Boekschoten, M.V., Verkade, H.J., et al. (2018). Sex differences in lipid metabolism are affected by presence of the gut microbiota. Sci. Rep. *8*, 13426. https://doi.org/10.1038/s41598-018-31695-w.

106. Volmer, R., van der Ploeg, K., and Ron, D. (2013). Membrane lipid saturation activates endoplasmic reticulum unfolded protein response transducers through their transmembrane domains. Proc. Natl. Acad. Sci. USA *110*, 4628–4633. https://doi.org/10.1073/pnas.1217611110.

107. Faust, P.L., and Kovacs, W.J. (2014). Cholesterol biosynthesis and ER stress in peroxisome deficiency. Biochim. Clin. *98*, 75–85. https://doi.org/10.1016/j.biochi.2013.10.019.

108. Kim, J., and Bai, H. (2022). Peroxisomal Stress Response and Inter-Organelle Communication in Cellular Homeostasis and Aging. Antioxidants *11*, 192. https://doi.org/10.3390/antiox11020192.

109. Hudry, B., de Goeij, E., Mineo, A., Gaspar, P., Hadjieconomou, D., Studd, C., Mokochinski, J.B., Kramer, H.B., Plaçais, P.Y., Preat, T., and Miguel-Aliaga, I. (2019). Sex Differences in Intestinal Carbohydrate Metabolism Promote Food Intake and Sperm Maturation. Cell *178*, 901–918.e16. https://doi.org/10.1016/j.cell.2019.07.029.

110. De Groef, S., Ribeiro Lopes, M., Winant, M., Rosschaert, E., Wilms, T., Bolckmans, L., Calevro, F., and Callaerts, P. (2024). Reference genes to study the sex-biased expression of genes regulating Drosophila metabolism. Sci. Rep. *14*, 9518. https://doi.org/10.1038/s41598-024-58863-5.

111. Millington, J.W., and Rideout, E.J. (2020). Sexual Dimorphism: Ecdysone Modulates Sex Differences in the Gut. Curr. Biol. *30*, R1327–R1330. https://doi.org/10.1016/j.cub.2020.08.088.

112. Shingleton, A.W., and Vea, I.M. (2023). Sex-specific regulation of development, growth and metabolism. Semin. Cell Dev. Biol. *138*, 117–127. https://doi.org/10.1016/j.semcdb.2022.04.017.

113. Zhu, Q., Qi, N., Shen, L., Lo, C.C., Xu, M., Duan, Q., Ollberding, N.J., Wu, Z., Hui, D.Y., Tso, P., and Liu, M. (2023). Sexual Dimorphism in Lipid Metabolism and Gut Microbiota in Mice Fed a High-Fat Diet. Nutrients *15*, 2175. https://doi.org/10.3390/nu15092175.

114. Meijer, B.J., Smit, W.L., Koelink, P.J., Westendorp, B.F., de Boer, R.J., van der Meer, J.H.M., Vermeulen, J.L.M., Paton, J.C., Paton, A.W., Qin, J., et al. (2021). Endoplasmic reticulum stress regulates the intestinal stem cell state through CtBP2. Sci. Rep. *11*, 9892. https://doi.org/10.1038/s41598-021-89326-w.

115. Heijmans, J., van Lidth de Jeude, J.F., Koo, B.K., Rosekrans, S.L., Wielenga, M.C.B., van de Wetering, M., Ferrante, M., Lee, A.S., Onderwater, J.J.M., Paton, J.C., et al. (2013). ER stress causes rapid loss of intestinal epithelial stemness through activation of the unfolded protein response. Cell Rep. *3*, 1128–1139. https://doi.org/10.1016/j.celrep.2013.02.031.

116. Niederreiter, L., Fritz, T.M.J., Adolph, T.E., Krismer, A.M., Offner, F.A., Tschurtschenthaler, M., Flak, M.B., Hosomi, S., Tomczak, M.F., Kaneider, N.C., et al. (2013). ER stress transcription factor Xbp1 suppresses intestinal tumorigenesis and directs intestinal stem cells. J. Exp. Med. *210*, 2041–2056. https://doi.org/10.1084/jem.20122341.

117. Rera, M., Clark, R.I., and Walker, D.W. (2012). Intestinal barrier dysfunction links metabolic and inflammatory markers of aging to death in Drosophila. Proc. Natl. Acad. Sci. USA *109*, 21528–21533. https://doi.org/10.1073/pnas.1215849110.

118. Guo, L., Karpac, J., Tran, S.L., and Jasper, H. (2014). PGRP-SC2 promotes gut immune homeostasis to limit commensal dysbiosis and extend lifespan. Cell *156*, 109–122. https://doi.org/10.1016/j.cell.2013.12.018.

119. Choi, N.H., Kim, J.G., Yang, D.J., Kim, Y.S., and Yoo, M.A. (2008). Age-related changes in Drosophila midgut are associated with PVF2, a PDGF/VEGF-like growth factor. Aging Cell *7*, 318–334. https://doi.org/10.1111/j.1474-9726.2008.00380.x.

120. Regan, J.C., Khericha, M., Dobson, A.J., Bolukbasi, E., Rattanavirotkul, N., and Partridge, L. (2016). Sex difference in pathology of the ageing gut mediates the greater response of female lifespan to dietary restriction. Elife *5*, e10956. https://doi.org/10.7554/eLife.10956.

121. Pinelli, M., Makdissi, S., Scur, M., Parsons, B.D., Baker, K., Otley, A., MacIntyre, B., Nguyen, H.D., Kim, P.K., Stadnyk, A.W., and Di Cara, F. (2024). Peroxisomal cholesterol metabolism regulates yap-signaling, which maintains intestinal epithelial barrier function and is altered in Crohn's disease. Cell Death Dis. *15*, 536. https://doi.org/10.1038/s41419-024-06925-x.

122. Peeters, A., Swinnen, J.V., Van Veldhoven, P.P., and Baes, M. (2011). Hepatosteatosis in peroxisome deficient liver despite increased beta-oxidation capacity and impaired lipogenesis. Biochimie *93*, 1828–1838. https://doi.org/10.1016/j.biochi.2011.06.034.

123. Pertea, M., Kim, D., Pertea, G.M., Leek, J.T., and Salzberg, S.L. (2016). Transcript-level expression analysis of RNA-seq experiments with HISAT, StringTie and Ballgown. Nat. Protoc. *11*, 1650–1667. https://doi.org/10.1038/nprot.2016.095.

124. Matyash, V., Liebisch, G., Kurzchalia, T.V., Shevchenko, A., and Schwudke, D. (2008). Lipid extraction by methyl-tert-butyl ether for high-throughput lipidomics. J. Lipid Res. *49*, 1137–1146. https://doi.org/10.1194/jlr.D700041-JLR200.

125. Koelmel, J.P., Kroeger, N.M., Ulmer, C.Z., Bowden, J.A., Patterson, R.E., Cochran, J.A., Beecher, C.W.W., Garrett, T.J., and Yost, R.A. (2017). LipidMatch: an automated workflow for rule-based lipid identification using untargeted high-resolution tandem mass spectrometry data. BMC Bioinf. *18*, 331. https://doi.org/10.1186/s12859-017-1744-3.

126. Xia, J., Sinelnikov, I.V., Han, B., and Wishart, D.S. (2015). MetaboAnalyst 3.0–making metabolomics more meaningful. Nucleic Acids Res. *43*, W251–W257. https://doi.org/10.1093/nar/gkv380.

STAR★METHODS

KEY RESOURCES TABLE

REAGENT or RESOURCE	SOURCE	IDENTIFIER
Antibodies		
Rabbit anti-P-eIF2α (Ser51) (119A11)	Cell Signaling	#3597
Mouse anti-Delta	DSHB	#C594.9B
Mouse anti-Prospero	DSHB	#MR1A
Mouse P-H3	Upstate Biotechnology	#06-570
Alexa Fluor secondary 555-anti rabbit	Thermo Fisher	#A-31572
Alexa Fluor secondary 555-anti mouse	Thermo Fisher	#A-31570
Chemicals, peptides, and recombinant proteins		
niacin	SIGMA ALDRICH	#481918
Nutrifly® mix	Genesee Scientific™	#66-116
Tofacitinib	SIGMA ALDRICH	# PZ0017
Batyl alcohol	SIGMA ALDRICH	#B402- 1G
DAPI Pro-Gold Antifade Reagent	Thermo Fisher Scientific	# P36931
Coconut oil	SIGMA ALDRICH	# 8001-31-8
Erucic acid	SIGMA ALDRICH	# 112-86-7
Bovine serum albumin (BSA)	SIGMA ALDRICH	#A3299
Pierce™ 16% Formaldehyde (w/v), Methanol-free	Thermo Fisher Scientific	#28906
Amplex Red Hydrogen Peroxide/ Peroxidase Assay Kit	Thermo Fisher Scientific	# A22188
Free Fatty Assay Kit	SIGMA ALDRICH	# MAK044-1KT
Qubit Protein Assay Kit	Thermo Fisher Scientific	# Q33211
PBS 10 X	Thermo Fisher Scientific	#70011044
Dimethyl sulfoxide	SIGMA ALDRICH	# 67-68-5
Critical commercial assays		
In Situ Cell Death Detection Kit, TMR red	SIGMA ALDRICH	#12156792910
Intesticult Organoid Growth Medium	STEMCELL Technologies	# 06005
Gentle Cell Dissociation Reagent	STEMCELL Technologies	# 07174
DMEM/F-12 with 15 mM HEPES	STEMCELL Technologies	# 36254
Bovine Serum Albumin solution	Millipore SIGMA	2-100M
Y-276632 (2HCL)	STEMCELL Technologies	#72302
GRO FACTOR RE/MATRIGEL MATRIX	Corning Inc	#356231
Deposited data		
RNAseq data ncbi accession number	This paper	Database NCBI: PRJNA1189839 This study
Experimental models:Strains		
Pex5-loxP mouse B6J.129-*Pex5*^{tm1Pec}/BaesJ	Jackson Laboratory	#031665
villin-Cre B6.Cg-Tg(Vil1-cre)1000Gum/J	Jackson Laboratory	#021504
Pex5-i *w[3] {w[+] VDRC. 14972* }GD	VDRC	# 42332
esg^{GFP} y[1],w[1]; esg-GAL4, UAS-GFP; Gal80ts	University of Alberta Foley's lab	NA
UAS-ERp60-i *y[1] sc[*] v[1] sev[21]; P{y [+t7.7] v[+t1.8] = TRiP.HMS00885}attP2*	BDSC	# 33935

(*Continued on next page*)

Continued

REAGENT or RESOURCE	SOURCE	IDENTIFIER
UAS-ERp60-i W[3]P{attP,w+,VDRC.6676'}KK	VDRC	#KK105601
UAS-ERp60^{OE}	Di Cara Lab Dalhousie University	This paper
W^{1118} w[1118]	BDSC	#5905
UAS-GFP w[1118]; P{w[+mC] = UAS-GFP.nls}8	BDSC	#4776
Acox1-i y[1] sc[*] v[1] sev[21]; P{y[+t7.7] v [+t1.8] = TRiP.HMC03620}attP40	BDSC	#52882
GNPAT-i y[1] sc[*] v[1] sev[21]; P{y[+t7.7] v [+t1.8] = TRiP.HMC03654}attP40	BDSC	# 52914
Xbp1-i y[1] sc[*] v[1] sev[21]; P{y[+t7.7] v [+t1.8] = TRiP.HMS03015}attP2.	BDSC	#36755
Xbp1-GFP w[*]; P{w[+mC] = UAS-Xbp1.EGFP.LG}4	BDSC	#39719
Xbp1OE *xbp1^{EP2112}*	Exelicis	#EP2112
Calr^{OE} y[1] w[*]; PBac{y[+mDint2] w[+mC] = UAS-hCALR.HA}VK00037/SM6a	BDSC	#84837
Cat-i y[1] sc[*] v[1] sev[21]; P{y[+t7.7] v [+t1.8] = TRiP.GL01541}attP40	BDSC	#43197
Dome-i y[1] v[1]; P{y[+t7.7] v[+t1.8] = TRiP.JF01682}attP2	BDSC	# 28983
Perk^{A} w-; PERK[deltaLD], vas-Cas9 (3xP3>GFP)/TM3Sb	Hurd lab University of Toronto	NA
Mex-Gal4 y P{w[+mC] = mex1-GAL4.2.1}9-1, y[1] w[1118]	BDSC	# 91367
Oligonucleotides		
See Table S2		
Recombinant DNA		
pTW-ERp60^{OE}	Di Cara Lab Dalhousie University	This paper
Software and algorithms		
Fijii software	NA	imagej.net (USA), micron.ox.ac.uk (European mirror)
Prism10	GraphPad	https://www.graphpad.com
HISAT2, StringTie, Ballgown and Deseq2	NA	Shingleton and Vea[112]
QIAGEN CLC Genomics Workbench	NA	https://digitalinsights.qiagen.com/trial-request
Qiagen GeneGlobe platform	Qiagen	www.qiagen.com/GeneGlobe
GSEA	NA	https://www.gsea-msigdb.org/gsea/index.jsp
Cytoscape	NA	https://cytoscape.org
Other		
Confocal microscope	ZEISS	LSM 880 with Airy scan
Costar® 24-Well Flat-Bottom Plate, Tissue Culture-Treated	STEMCELL Technologies	# 38017

EXPERIMENTAL MODEL AND STUDY PARTICIPANT DETAILS

Drosophila melanogaster

All fly stocks were maintained at either 18°C or 25°C on standard Bloomington cornmeal medium. F1 males and females used for experiments were moved to 29 °C at larval stage 1 and kept for 3, 10 or 14 days post eclosion, depending on the experiment, before

being dissected. Males and Females analyzed in the survival assay were moved to 29 °C at larval stage 1 and kept until death. The initial transcriptomic screen was performed on midguts dissected from 10-day-old flies (100 males and 100 females together to obtain 200 guts per replicate). QRT-PCR experiments to validate the RNAseq results were performed in 10-day-old flies that were moved to 29°C as L1 larvae.; males and females were separated for the experiment. All other experiments were performed using 3-10-day-old or 14-old flies. The initial Q-PCR and fluorescence microscopy experiments to validate the results of the RNA screen and identify gene hits were performed on males and females separated. Follow-up experiments were performed on pooled males and females when sex-specific differences were not identified. The sex of flies for each experiment is reported in the figures. For rescue experiments, the parental crosses were set to generate flies carrying two constructs needed to promote RNA-mediated depletion or overexpression of each gene of interest together with the temperature-sensitive inducible driver (*w; esgGal4, tub-Gal80^{TS}; UAS-GFP*), flies carrying individual recombinant construct to manipulate one gene of interest and the temperature-sensitive inducible driver or only the temperature-sensitive inducible driver; guts from each of these groups were compared in each biological replicate. For all the other crosses, experimental F1 was compared to F1 of control crosses that were individually set.

Our team generated the *pTW-ERp60^{OE}* strain for this study. The recombinant DNA was made by first amplifying the cDNA sequence coding for the ERp60 ERp60-Forward 5′- C ACC ATG ATG TGG CGC CTT and ERp60-Reverse 5′- TTA GAG CTC GGT CTT CTT GGG. The amplified fragment was cloned into the pENTR/D-TOPO donor vector (Thermo Fisher) and then transferred to the *Drosophila* Gateway destination vector, pTW.

The recombinant DNA was sent to Genome ProLab Sherbrooke, Québec, Canada to generate transgenic flies.

All the strains used in this study are reported in the key resources table.

Ethics approval and consent to participate

Mouse colonies were maintained as stable inbred lines under the Dalhousie University committee for laboratory animals' institutionally approved animal protocol # 24-014, abiding by the standards of the Canadian Council on Animal Care.

Pex5 mutant mice

The Pex5-loxP mouse (B6J.129-*Pex5^{tm1Pec}*/BaesJ, Jackson Laboratory)[122] contains *loxP* sites flanking exons 11–14 of the *Pex5* gene, and deletion of the floxed sequence creates a null allele. The villin-Cre mouse (B6.Cg-Tg(Vil1-cre)1000Gum/J, Jackson Laboratory) carries a Cre recombinase expressed under the control of the villin promoter. This enables targeted spatiotemporally controlled *Pex5* deletion in the gut in the villus and crypt epithelial cells of the small and large intestines. Heterozygous were crossed to obtain vilCre/VilCre; Pex5$^{-/-}$ mice.

We used 2-day-old male and female mice to grow the organoids.

METHOD DETAILS

Cornmeal diet (CMD)

The CMD food was prepared following the Bloomington stock center recipe (https://bdsc.indiana.edu/information/recipes/bloomfood.html). The liquid food was then poured into a DrosoFiller (Flystuff 59–168 Droso-filler, Narrow, Genesee Scientific) for mass dispensing into polypropylene 46 mL housing vials.

High-fat diet (HFD)treatment

Adult 3-day-old flies were fed High-fat food (HFD) for 24 h (h). HFD was made using a 4:1 ratio of cornmeal food to fat. For 5mL final volume of HFD food, 4 mL of Cornmeal food was mixed with 750 μL of Coconut oil and 250 μL Erucic acid. The CM food was freshly prepared as described above and then mixed with the two lipids warmed at 50°C. Ten μL blue food colors were added to the mixture to monitor the HFD food's homogeneity and allow the selection of well-fed flies before dissection. The choice of fats was made to obtain a mixture of Long Chain Fatty Acids (LCFAs) (coconut oil) and Very Long Chain Fatty Acids (VLCFAs) (erucic acid).

1-*O*-Octadecyl-*rac*-glycerol treatment

Adult 3-day-old flies were fed CM food supplemented with 1-*O*-Octadecyl-*rac*-glycerol (Batyl alcohol) at a final 1 mg/ml concentration for 4 days at 29°C. As 1-*O*-Octadecyl-*rac*-glycerol is soluble in 5% Chloroform, we analyzed the flies on CM food supplemented with 5% Chloroform as a control.

Niacin treatment

Adult 3-day-old flies were fed CM food supplemented with niacin (nicotinic acid) 0.100g/100 mL (N4126, Sigma-Aldrich) at every life cycle stage and tested 7 days after eclosion.

Tofacitinib treatment

Adult 5-day-old flies were fed CM food supplemented with 18 mM Tofacitinib for 2 days days at 29°C. As Tofacitinib is soluble in DMSO, we analyzed the flies on CM food supplemented with DMSO as a control.

Survival assay

To generate survival curves for flies with knockdowns of *Xbp1*, *ERp60, or Pex5 in PG (esg*-driven knockdown*) and relative control (esgGFP>w1118),* adult male and female flies were collected and kept for 48 h at 25°C to mate. On the third day, male and female flies were anesthetized with CO2 and divided by sex in the group on regular CM food. Survival experiments were done at 29°C with 20 flies for each group. Surviving flies were transferred daily to fresh vials and counted.

Measurement of H_2O_2

For H_2O_2 measurement, 20 guts from flies of each genotype or under specific conditions were homogenized in PBS and clarified by centrifugation. H_2O_2 amounts in the resultant supernatants were measured using the Amplex Red Hydrogen Peroxide/Peroxidase Assay Kit (Thermo Fisher) and normalized to protein amounts. Protein amounts were measured using a Qubit II fluorimeter (Thermo Fisher). Experiments were done in triplicate.

Free fatty acids (FFA) quantification

For FFA measurement, 20 guts from flies of each genotype or under specific conditions were homogenized in PBS and clarified by centrifugation. FFA quantification was done using the Free Fatty Assay Kit (Sigma) following the manufacturers' protocols. Lipid amounts were normalized to protein amount. The protein concentration in the lysates was determined using the Qubit Protein Assay Kit (Thermo Fisher), according to the manufacturer's instructions.

Progenitors (ISC and EB) isolation, RNA extraction and library preparation for RNA sequencing transcriptomic

Intestinal stem cell isolation by fluorescence-activated cell sorting (FACS) was adapted from the published protocol article by *Dutta* et al*., 2013*. In brief, three biological replicates consisting of 200 fly guts per replicate were dissected in PBS-1X and then immediately transferred into a 1.5-mL microcentrifuge tube containing ice-cold diethylpyrocarbonate (DEPC)-treated water-PBS (400 μL). Dissected midguts were then dissociated with 100 μL elastase solution (1 mg/mL final concentration) and incubated for 1 h at 27°C in a heating block with shaking at 34 × g. Dissociated cells were centrifuged for 20 min at 300 × g, at 4°C, and the pellets were resuspended in 500 μL fresh PBS-DEPC for sorting. 1 μL of 1 mg/mL propidium iodide was added, and then dissociated cells were filtered using 25-μm filters to remove clumps. Cell suspension was then FACS sorted. GFP^+ cells from the $esg^{GFP}>w^{1118}$ and w^{1118} (negative control no GFP) midguts flies were sorted out first to set the fluorescence gate. For each of the three biological replicates, about 40,000 GFP^+ cells were sorted. RNA was isolated from the FACS-sorted GFP^+ cells using a Direct-zol RNA Microprep kit, followed by library preparation using the QIAseq UPX3′ transcriptome for next-generation sequencing paired to the QIAseq UPX 3′ trans. 12 (Index 48). Libraries were pooled and quantified using QIAseq library Quant Assay kit and analyzed on a bioanalyzer (Agilent). Libraries were sent to Center d'expertise et de services Génome Québec, where they were sequenced using NovaSeq6000 SP flowcell using custom primers from the QIAseq UPX3 transcriptome kit.

RNA sequencing analyses

The differentially expressed genes were determined using three different pipelines, and the results were compared. The fastQ files were analyzed using.

(1) the Qiagen GeneGlobe platform (www.qiagen.com/GeneGlobe).
(2) The QIAGEN CLC Genomics Workbench.
(3) The HISAT2, StringTie, Ballgown and Deseq2 pipeline, as reported previously.[123]

RNA-seq enrichment pathway

Gene Set Enrichment Analysis (GSEA) was performed using GSEA v4.1.0 to identify biological processes, cellular components, and KEGG pathways significantly altered in the intestinal progenitors of $esg^{GFP}>Pex5\text{-}i$ versus $esg^{GFP}>w^{1118}$ midguts. The gene interaction network of GSEA results was generated and manually curated to remove redundant and uninformative nodes using Cytoscape v3.8.2.73.

Total RNA extraction, cDNA synthesis and QRT-PCR

Midguts from adult flies were dissected in Phosphate-buffered saline (PBS-1X), transferred to TRIzol reagent, and snap-frozen in dry ice. Total RNA was extracted using the Direct-zol RNA Microprep kit following the manufacturer's protocol. RNA was reverse transcribed using the High-capacity Script cDNA Synthesis kit, and the synthesized cDNA was amplified by QPCR using the SYBR-Green PCR master mix using a QuantStudio 6 Flex qPCR machine (Applied Biosystems, Thermo Fisher Scientific). Samples were normalized to *Rpl23* gene expression, the relative quantification methods, and primer efficiency. Primer sequences used in real-time qPCR are presented in the key resources table. In some experiments, data were represented as % of relative expression compared to the control condition.

RT-PCR to test XBp1 splicing

Total RNA was isolated from esg^{GFP}>*Pex5-i* versus esg^{GFP}>w^{1118} midguts. One microgramme of isolated RNA using Direct-zol RNA Microprep kit was reverse transcribed using the High-capacity Script cDNA Synthesis kit. The synthesized cDNA was amplified by PCR using the 2X Q5 master mix. The PCR products were detected on 2% agarose gel by electrophoresis. The band's intensity ratio indicated the differentially spliced Xbp1 mRNA (220 bp) to the inactive spliced form of Xbp1 mRNA (240 bp) was calculated in each sample to determine the amount of active Xbp1 per sample and condition. *Rpl23* was used as a loading control to calculate the band's intensity ratio of the spliced Xbp1 to Rpl23. The bands' intensity was calculated using the open-source FIJI software package.

Immunofluorescence and confocal microscopy

Guts were fixed in 4% paraformaldehyde in PBS-1x for 45 min, washed three times (15 min each) in PBS-T (PBS containing 0.05% Triton X-100), and incubated for 1 h at room temperature in blocking solution (5% Bovine fetal serum in PBS-T) and incubated with primary antibody in blocking solution for 16 h at 4°C. Rabbit anti-P-eIF2α antibody was used at 1:250 dilution, mouse anti-P-H3, mouse anti-Prospero and mouse anti-Delta were used at 1:100. Tissues were then washed three times in PBS-T and incubated in the appropriate Alexa Fluor secondary 555-anti rabbit IgG or 555-anti mouse IgG antibodies at 1:1000 dilution and 4′,6-diamidino-2-phenylindole (DAPI) at 1:1000 dilution. After three washes in PBST, and one last wash in PBS-1x, guts were mounted in Prolong-Gold Antifade Reagent and imaged using a 20× or a 40× plan-Apochromat lens mounted onto an Axio-Observer M1 microscope (Zeiss).

Post-imaging analysis was performed using the open-source Fijii software package or ZEN software. The analyzed region of interest (ROI region) represents a 425.10 × 425.10 micron in the posterior midguts. Multiple ROI regions were taken to cover the entire posterior midgut and the average value per posterior midgut was reported as a single dot/fly. At least ten guts were imaged for every genotype and/or condition in every experiment, and representative images were chosen for each experiment.

Detection of apoptosis assay

In Situ cell death detection kit, TMR red assay was used for the detection and quantification of apoptotic cell death in midguts. The reaction preferentially labels DNA strand breaks generated during apoptosis. 10 μL of Enzyme Solution were added to 90 μL Label Solution to obtain 100 μL TUNEL reaction mixture (working solution). The TUNEL reaction mixture should be prepared immediately and kept on ice until use. Midguts were dissected, in 4% paraformaldehyde in PBS-1x for 45 min, washed three times (15 min each) in PBS-T (PBS containing 0.05% Triton X-100), then incubated with the TMR working solution for 30 min in the dark with slow shaking. Guts were then washed 2 times (15 min each) in PBS-T then incubated with DAPI at 1:1000 dilution for 45 min. After three washes in PBST and one wash with PBS-1X, guts were mounted in Prolong-Gold Antifade Reagent (Thermo Fisher) and imaged using a 20× objective mounted onto an Axio-Observer M1 microscope (Zeiss).

Smurf assay

10-day-old female and male flies were moved from regular cornmeal food to vials containing a vial plug saturated with a solution of 5% sucrose in PBS plus blue food coloring. After 48 h the flies were imaged with a 12.4× magnification on a SteREO Discovery V20 Microscope, equipped with an Axiocam 208 color camera (Zeiss). Image analysis was performed in ImageJ.

Lipidomics

Lipid Extraction

Extraction of lipids was carried out using a biphasic solvent system of cold methanol, methyl *tert*-butyl ether (MTBE), and PBS/water[124] with some modifications. In a randomized sequence, to each sample was added 225 μL MeOH with internal standards and 188 μL PBS. Samples were homogenized for 30 s, transferred to 1.5 mL Eppendorf tubes containing 750 μL MTBE, and then incubated on ice with occasional vortexing for 1 h. Following incubation, samples were centrifuged at 15,000 × g for 10 min at 4°C. The organic (upper) layer was collected, and the aqueous (lower) layer was re-extracted with 1 mL of 10:3:2.5 (*v/v/v*) MTBE/MeOH/dd-H2O, briefly vortexed, incubated at RT, and centrifuged at 15,000 × g for 10 min at 4°C. Upper phases were combined and evaporated to dryness under speedvac. Lipid extracts were reconstituted in 400 μL of 4:1:1 (v/v/v) IPA/ACN/water and transferred to an LC-MS vial for analysis. Concurrently, process blank samples were prepared and pooled quality control (QC) samples were prepared by taking equal volumes (150 μL) from each sample after final resuspension.

Mass spectrometry analysis of samples

Lipid extracts were separated on an Acquity UPLC CSH C18 column (2.1 × 100 mm; 1.7 μm) coupled to an Acquity UPLC CSH C18 VanGuard precolumn (5 × 2.1 mm; 1.7 μm) (Waters, Milford, MA) maintained at 65°C connected to an Agilent HiP 1290 Sampler, Agilent 1290 Infinity pump, and Agilent 6545 Accurate Mass Q-TOF dual AJS-ESI mass spectrometer (Agilent Technologies, Santa Clara, CA). Samples were analyzed in a randomized order in both positive and negative ionization modes in separate experiments acquiring with the scan range m/z 100–1700. For positive mode, the source gas temperature was set to 225°C, with a drying gas flow of 11 L/min, nebulizer pressure of 40 psig, sheath gas temp of 350°C and sheath gas flow of 11 L/min. VCap voltage is set at 3500 V, nozzle voltage 500V, fragmentor at 110 V, skimmer at 85 V and octopole RF peak at 750 V. For negative mode, the source gas temperature was set to 300°C, with a drying gas flow of 11 L/min, a nebulizer pressure of 30 psig, sheath gas temp of 350°C and sheath gas flow 11 L/min. VCap voltage was set at 3500 V, nozzle voltage 75 V, fragmentor at 175 V, skimmer at 75 V and octopole RF

peak at 750 V. Mobile phase A consisted of ACN:H_2O (60:40, *v/v*) in 10 mM ammonium formate and 0.1% formic acid, and mobile phase B consisted of IPA:ACN:H_2O (90:9:1, *v/v/v*) in 10 mM ammonium formate and 0.1% formic acid. For negative mode analysis the modifiers were changed to 10 mM ammonium acetate. The chromatography gradient for both positive and negative modes started at 15% mobile phase B then increased to 30% B over 2.4 min, it then increased to 48% B from 2.4–3.0 min, then increased to 82% B from 3–13.2 min, then increased to 99% B from 13.2–13.8 min where it's held until 16.7 min and then returned to the initial conditions and equilibrated for 5 min. Flow was 0.4 mL/min throughout, with injection volumes of 7 μL for positive and 10 μL negative mode. Tandem mass spectrometry was conducted using iterative exclusion, the same LC gradient at collision energies of 20 V and 27.5 V in positive and negative modes, respectively.

Analysis of mass spectrometry data

For data processing, Agilent MassHunter (MH) Workstation and software packages MH Qualitiative and MH Quantitative were used. The pooled QC (n = 8) and process blank (n = 4) were injected throughout the sample queue to ensure the reliability of acquired lipidomics data. For lipid annotation, accurate mass and MS/MS matching was used with the Agilent Lipid Annotator library and LipidMatch (See Ref below). Results from the positive and negative ionization modes from Lipid Annotator were merged based on the class of lipid identified. Data exported from MH Quantitative was evaluated using Excel where initial lipid targets are parsed based on the following criteria. Only lipids with relative standard deviations (RSD) less than 30% in QC samples are used for data analysis. Additionally, only lipids with background AUC counts in process blanks that are less than 30% of QC are used for data analysis. The parsed excel data tables are normalized based on the ratio to class-specific internal standards, then to tissue mass and sum prior to statistical analysis.[125]

Statistical analysis

Multivariate analysis was performed using MetaboAnalyst. Statistical models were created for the normalized data after normalizing to sum, logarithmic transformation (base 10) and Pareto scaling.[126]

Mouse intestinal organoids culture

The protocol for crypt isolation is adapted from the one available at the STEMCELL Technologies (Vancouver, BC) Website. All the solutions, except for the Intesticult Organoid Growth Medium (STEMCELL Technologies), were kept on ice and used cold. On day 0, the pups were sacrificed through decapitation, and the small and large intestines were harvested in cold sterile 1X PBS. After 2 washes with cold 1X PBS, the tissue was minced in the smallest pieces possible with sterile scissors inside the tube. The pieces were washed 3 more times and incubated with 10 mL of Gentle Cell Dissociation Reagent (STEMCELL Technologies) for 15 min at RT on a rocking platform. After washing with 1X PBS plus 0.1% BSA the fragments were passed through a 70 mm filter, and then washed again in DMEM/F-12 with 15 mM HEPES (STEMCELL Technologies). The crypts were resuspended in a cold solution made of ½ Growth Factor Reduced Matrigel (Corning Inc., Corning, NY, USA) and ½ DMEM/F-12 (STEMCELL Technologies) and seeded in 50 mL drops in a pre-warmed 24-well plate (Corning Inc.). The seeding concentration was 200 crypts/dome. The plate was incubated for 10 min at 37°C to let the Matrigel polymerize, and then the pre-warmed complete Intesticult Organoid Growth Medium was added, 500 mL per well. Media changes were performed every two days, and organoids were passaged approximately once a week at a 1:4-1:6 ratio.

QUANTIFICATION AND STATISTICAL ANALYSIS

Statistical analyses

All statistical analyses were done in Prism (Graph-Pad). All data were assessed for normality using Shapiro–Wilk checks before running statistical tests. Statistical significance was determined using a two-tailed Student's t test, one-way analysis of variance (ANOVA), two-way ANOVA, or using the Kaplan–Meier log rank for survival assays. Significance is shown in figures as ns; $*p \leq 0.05$; $**p \leq 0.01$; $***p \leq 0.001$; $****p \leq 0.0001$. The statistical details of experiments can be found, including the statistical tests used, the exact value of n, and dispersion and precision measures are reported in the figure legends.

Quantification of agarose gel band signals

To determine the density of bands on a agarose gel, we used FIJI using the protocol reported in (https://imagej.nih.gov/ij/docs/menus/analyze.html#gels). In brief.

(1) File>Open
(2) The gel analysis routine requires the image to be a gray-scale image. To convert to grayscale, go to Image>Type>8-bit.
(3) Use the rectangular selection tool to outline the first lane. The rectangle should be tall and narrow to enclose a single road.
(4) Select*Analyze>Gels>SelectFirstLane*(orpress"1″),andthelanewillbeoutlinedand"Lane1selected"displayedinthestatus bar.
(5) Move the rectangular selection right to the next lane and select *Analyze>Gels>Select Next Lane* (or press "2″). The designated lane is outlined and labeled, and "Lane n selected" is displayed in the status bar.
(6) Repeat the previous step for each remaining lane.
(7) Select *Analyze>Gels>Plot Lanes* (or press "3″) to generate the lane profile plots.
(8) Use the straight-line selection tool to draw baselines and drop lines so that each peak of interest defines a closed area.

(9) For each peak, measure the size by clicking inside with the wand tool.
(10) Select *Analyze>Gels>Label Peaks* to label each measured peak with its size as a percent of the total length of the measured peaks.
(11) The values from the Results window can be moved to an Excel spreadsheet program to calculate the ratio between the density of a protein of interest over the density of a protein used as loading control for each sample and treatment.

Quantification of GFP+ cells in midguts

The number of cells expressing GFP or positive for Delta antibody or TUNEL staining were counted using Fiji's. The quantification was done by manually counting the number of positive-stained cells within a region of Interest field (ROI) fixed across the samples and reported as the number of cells/ROI.

Quantification of fluorescence signals

To determine the intensity of the defined protein within the cell.

(1) Open the ImageJ software.
(2) Click the 'File' tab, then click 'Open' to open the file you want to quantitate. A window will pop up named 'Bio-Format Import Options.'
(3) 'Hyperstack' and 'Colorized' options allow independent analysis of each fluorescent channel collected in the original experiment.
(4) Click on the Split channels to obtain three separated windows one for each of the three color channels so that the quantitation of each fluorescent channel can be performed separately.
(5) Hit 'OK' at the bottom right of the window to proceed to the next quantification step.
(6) Click on the 'Freehand selections' button and then use the drawing pen to circle the area of the cell to be quantitated.
(7) Click the 'Analyze' button to select the 'Measure' option. A window will then pop up named 'Results,' which includes several measurements that the software made on the chosen area, including Median Intensity. Copy the median value in an Excel sheet for each gut measured. Measure at least 10 guts.

It is preferable to subtract the background Median Fluorescence Intensity (MFI) from the MFI of a region of interest (ROI) while analyzing images since the background of an image might affect the MFI quantitation.

(1) Repeat step 7 to select and measure a non-fluorescent area of the same image. MFI of that non-fluorescent area/negative control image is then subtracted from the tissue area MFI.
(2) Calculate the final MFI = MFI of an ROI – MFI of Background.
(3) Copy and paste the value in Prism to represent results in a diagram and carry out our statistical analyses.